Journal of Alloys and Compounds 1034 (2025) 181316

Contents lists available at ScienceDirect

Journal of Alloys and Compounds

journal homepage: www.elsevier.com/locate/jalcom

Machine learning approach to the possible synergy between co-doped elements in the case of $LiFePO_4/C$

Z.M.S. Elbarbary [a,b], Priya A. Hoskeri [c,*], Ali A. Javidparvar [d,*], Mohammed M. Alammar [a,b], Amuthakkannan Rajakannu [e], Theodore Azemtsop Manfo [f,*]

[a] Department of Electrical Engineering, College of Engineering, King Khalid University, P.O. Box 394, Abha 61421, Saudi Arabia
[b] Center for Engineering and Technology Innovations, King Khalid University, Abha 61421, Saudi Arabia
[c] VTU Research Center, Department of Physics, Dayanand Sagar College of Engineering, Kumarswamy Layout, Bangalore 560 078, India
[d] School of Metallurgy and Materials Engineering, College of Engineering, University of Tehran, P.O. Box 11155-4563, Tehran, Iran
[e] Department of Mechanical and Industrial Engineering, National University of Science and Technology, Muscat, Oman
[f] Department of Electrical Engineering and Energy Technology, School of Technology and Innovations, University of Vaasa, Wolffintie 32, Vaasa 65200, Finland

ARTICLE INFO

Keywords:
Co-doping
Li-ion batteries
Machine Learning
Synergic effects
LFP

ABSTRACT

This study investigates the synergistic effects produced by the co-doping of several components in the LFP/C structure. To execute this work, a dataset was initially created from the existing literature, encompassing information on doped LFP structures by a singular element. Numerous intrinsic and extrinsic characteristics, such as atomic number, valence, relative variations in atomic and ionic radii of Fe and Li, electronegativity, molar percentage of dopant, and C-rate, were evaluated. The optimal selection of features leading to satisfactory model training was achieved by analyzing the Pearson correlation coefficient factors. Subsequently, two machine learning algorithms (i.e., Random Forest and Gaussian Process Regression) were trained using the optimized feature set. The two models were evaluated, and the model with superior predictive power was chosen for further study. An analysis of the synergistic effect of two co-dopants was conducted by comparing the actual specific discharge capacities with the expected values derived from the superimposition of the machine learning predictions. Ultimately, experimental validation was conducted by synthesizing several unique $LiY_xNd_yFe_{1-x-y}PO4/C$ (Nd = 0.06, 0.02 <Y<0.08) samples using solid-state methods. The synthesized powders underwent relevant testing, including SEM, TEM, CV, EIS, and GD. Finally, based on the best ML scheme developed and experimental results, another ML scheme was developed to analyze the possible synergic effects that co-dopants may exhibit regarding the specific discharge capacity of co-doped LFP structures.

1. Introduction

For the chemical storage of electricity, there are two categories of batteries: (a) primary (non-rechargeable) batteries and (b) secondary (rechargeable) ones. Commercially produced secondary batteries include LA (lead-acid), Ni-Cd (nickel-cadmium), LiMH (nickel-metal hydride), LiBs and SiBs (sodium-, and lithium-ion batteries) [1–7]. Cost-effective and secure energy storage is crucial for the effective implementation of electronic and electrical appliances and equipment, with rechargeable batteries emerging as a prominent solution [8,9], especially within renewable energy systems. LiBs stand out as the most efficient and versatile technology, providing exceptional energy and current density, elevated voltage, and extended life cycles that can surpass 1000 cycles. In this regard, they have emerged as the favored alternative to outdated technologies like LA and Ni-Cd. Recent advancements, including new electrode materials [10,11] and innovative synthesis methods, further enhance their applicability for renewable energy storage, making them indispensable in modern energy systems [12–17].

Among different elements of LiBs, the cathode, given its lower specific capacity, is the major element influencing the energy density [18]. Furthermore, the primary factor constraining the charge rate in these batteries is the rate of Li^+ ion diffusion within the cathode [19–22]. A range of materials has been utilized as cathodes in LiBs up to this point. A good cathode material should possess characteristics such as high capacity, good cycle life, stability, non-toxicity, high purity, and ease of

* Corresponding authors.
E-mail addresses: priya-physics@dayanandasagar.edu (P.A. Hoskeri), Javidparvar@ut.ac.ir (A.A. Javidparvar), theodore.azemtsop.manfo@uwasa.fi (T.A. Manfo).

https://doi.org/10.1016/j.jallcom.2025.181316
Received 3 February 2025; Received in revised form 5 April 2025; Accepted 30 May 2025
Available online 2 June 2025

manufacturing [22–24]. To achieve the desired characteristics, the produced cathode material must possess properties such as small particle size, uniform particle distribution and morphology, high crystallinity, high specific surface area, and minimal defects and agglomeration [25–27]. In this essence, $LiFePO_4$ (LFP) can be considered the primary candidate for LiB cathodes via its desirable thermal stability, affordability, non-toxic sources, and availability [28–30]. Among the most prominent advantages of $LiFePO_4$ are the stability of its structure during lithium-ion insertion and removal and its wide voltage range. Nonetheless, it has certain limitations, such as a low ionic diffusion coefficient ($10^{-12} - 10^{-11}$ cm^2/s) resulting from the one-dimensional movement of Li^+ within the structure, as well as poor electrical conductivity (10^{-10} S/cm) [29,31,32].

To address the above-mentioned challenges associated with LFP, techniques such as minimizing grain size and ensuring a uniform particle size distribution, implementing carbon coatings, combining carbon coatings with an electron-conductive material, refining the morphology and shape of particles via low-temperature synthesis methods, and introducing multivalent cation doping can enhance the electronic conductivity and lithium mobility within the LFP structure [33–35]. The reduction of particle size has been utilized in numerous studies as a successful approach to enhance the capacity at elevated charge/discharge rates and stability during the cycling of LFP [36–38]. Many researchers believe that the reduced capacity of LFP at high charge/-discharge rates stems from its poor ionic conductivity [39–42]; hence, minimizing the particle size can potentially improve its electrochemical performance. The enhancement can be linked to the reduced pathways that enable quicker transport of ions and electrons, resulting in improved rate capabilities and cycling stability [37,43,44].

Apart from the particle size, incorporating doping elements into the LFP composition can enhance its capacity, cyclic stability, conductivity, and Li^+-ion diffusion coefficient. The doped elements include multivalent cations such as Nb^{5+}, Zr^{4+}, Ti^{4+}, Mg^{2+}, Cr^{3+}, V^{5+}, Cu^{2+}, and anions such as F^- and Cl^- [45–48]. In fact, by doping elements into the LFP structure, due to the creation of lattice defects, the mobility of Li^+-ions is increased [49,50]. On the other hand, due to the change in the capacity of Fe^{2+} to Fe^{3+} during charging/discharging, the structure of LFP consistently transitions from p-type to n-type semiconductor and vice versa. This phenomenon can be significantly enhanced by adding elements with valence electrons different from those of Li and Fe [51,52]. As a result, the addition of elements to the LFP composition can lead to increased ionic/electric conductivity. On the other hand, there exist several studies, albeit much more limited, in the literature aiming at investigating the effect of doping the LFP structure with more than a single element. In this manner, the works of Li et al. [53] on the addition of P and B, Kandhasamy et al. [54] on the addition of P and Si, Zhang et al. [55] on the addition of Ce and La, Tian et al. [56] on the addition of Ti and Nb, Gao et al. [57] on the addition of Zr and Co, Wang et al. [58] on the addition of Na, P, and Cl, and Li et al. [59] on the addition of V, F, and P can be mentioned.

Additionally, coating of LFP particles with carbon can enhance the surface conductivity of particles, allowing for the complete use of active materials even under high current densities [60–62]. Moreover, the application of carbon coating effectively restricts particle growth throughout the synthesis process, leading to a decrease in the particle size. Furthermore, carbon can function as an antioxidant to inhibit the conversion of Fe^{2+} to Fe^{3+} during synthesis, thus removing the necessity for a reducing atmosphere during the synthesis process [63,64].

As noted above, incorporating additional elements into the cathode active material composition is a strategy to enhance the efficiency of this material. In this regard, a nearly uncountable amount of articles can be found in the literature aiming at enhancing the performance of LFP through doping/co-doping this structure with various elements. However, despite these efforts, there is a substantial need for methods to study the concurrent effect of various factors on the performance of modified LFP structures. Due to the diversity of the available data, processing this information manually seems to be impossible. In this regard, machine learning methods can accomplish this task more efficiently, and in fact, these methods have been used actively in the literature for innovative material development purposes [65–67]. Recent literature emphasizes the role of machine learning in accelerating the discovery and optimization of Li-ion battery materials. For example, Wang et al. used gradient boosting and SHAP analysis to predict the discharge capacities of doped NCM cathodes, highlighting the influence of dopant features like lithium content and electronegativity [68]. Lv et al. reviewed ML applications for predicting and designing electrode/electrolyte materials, classifying ML methods into descriptive, predictive, and prescriptive categories and discussing their integration with battery state monitoring [69]. Alzamer et al. emphasized AI's potential for electrolyte discovery, advocating for frameworks that integrate structure-property relationships with ML models [70]. Deeg et al. proposed a novel image-based approach that leverages CNNs to directly predict the rate capability of LIB electrodes from light microscopy images of their microstructure, bypassing traditional feature extraction processes [71]. Additionally, in a comprehensive review, Valizadeh and Amirhosseini highlight the transformative impact of machine learning (ML) techniques across the entire lifecycle of lithium-ion batteries (LIBs), including design, manufacturing, performance evaluation, and recycling [72]. These studies underscore the potential of ML not only for performance prediction but also for uncovering hidden relationships, which aligns with the goal of identifying synergistic effects in co-doped LFP/C systems.

In this study, a dataset containing data regarding the efficiency of several doped elements in the enhancement of LFP/C's specific discharge capacity was gathered. Then, by studying the correlation between the input-input and input-output pairs, the most proper input features capable of serving the training of ML models were selected. In the next step, two machine learning schemes were developed, and the best one, in terms of its accuracy, was selected for further studies. In order to study the possible synergic effects between two co-doped elements, first, synergy was defined as the deviation of the performance of a co-doped LFP/C material from that attained by summing the individual effect of each dopant. In this manner, to calculate the latter, the above-mentioned developed ML scheme was employed. Afterward, through the comparison of the summed effect of individual dopants with actual values, the difference between these two parameters was further studied. This difference was approached by another ML scheme that was inspired by the ML scheme developed earlier. In this manner, the functional relationship between the best set of features of both dopants and the above-mentioned deviation was found. Finally, to validate this process, a novel co-doped LFP/C cathode material was synthesized and utilized as a validation. In this regard, the present work consists of three phases, namely 1) ML study of the effect of single elements on the performance of doped LFP structures to facilitate the study of the possible existence of a synergic effect between co-doped elements, 2) Fabrication and synthesize of a novel co-doped LFP cathode active material, and 3) Approaching the possible synergic effects between co-dopants through ML and by employing the data obtained from previous steps.

2. Materials and method

2.1. Machine learning overview

An ML framework was developed to forecast the precise discharge capacity of doped LFP/C specimens. The methodology employed was organized in the subsequent manner, as can be seen in Figure (a):

- **Development of a dataset**

A dataset was constructed by gathering data from the current literature, with a specific emphasis on various LFP/C compositions that have been doped with different elements at varying concentrations. The

dataset documented:

- o The chemical compositions of LFP/C samples are detailed.
- o The elements used for doping and their respective concentrations.
- o The C-rate at which galvanostatic discharge tests were conducted
- o The associated electrochemical performance (i.e., SDC).

This step was essential since it is a well-acknowledged fact that the precision and ability to generalize of machine learning models were influenced by the quality and variety of the dataset.

- **Selection of input features**

The model took into account various physicochemical properties of the doped element and the test conditions as input features, with the goal of understanding their impact on the specific discharge capacity, including:

- o **Z**: The atomic number of the doped element signifies its essential identity.
- o **V**: The valence of the doped element significantly influences its interactions within the LFP structure.
- o $\boldsymbol{\Delta r_{Fe\_ion}} = \left(r_{dopant\_ion} - r_{Fe\_ion}\right)/r_{Fe\_ion} \times 100\%$: The difference in ionic radius between the doped element and iron influences lattice distortion, phase stability, and the pathways for lithium-ion diffusion.
- o $\boldsymbol{\Delta r_{Li\ \&\ ion}} = \left(r_{dopant\_ion} - r_{Li\_ion}\right)/r_{Li\_ion} \times 100\%$: The variation in ionic radius between the doped element and Li is similar to the previous point.
- o $\boldsymbol{\Delta r_{Fe\_atom}} = \left(r_{dopant\_atom} - r_{Fe\_atom}\right)/r_{Fe\_atom} \times 100\%$: The variation in atomic radius between the doped element and Fe highlights the possible impacts of lattice strain.
- o $\boldsymbol{\Delta r_{Li\_atom}} = \left(r_{dopant\_atom} - r_{Li\_atom}\right)/r_{Li\_atom} \times 100\%$: The variation in atomic radius between the doped element and Li is similar to the aforementioned.
- o The **mol%** of the doped element indicates the level of doping present.
- o The **C-rate** indicates the rate at which charging or discharging occurs, influencing the electrochemical performance.
- o The electronegativity, χ, of the doped element significantly influences electronic conductivity and redox potential.

In this context, considering that Δr_{Fe_ion}, Δr_{Li_ion}, Δr_{Fe_atom}, and Δr_{Li_atom} exhibit linear correlation, selecting all of them as input variables might appear unnecessary. Nonetheless, the rationale for this choice can be articulated in the following manner:

1. *What was the rationale for selecting variations in both atomic and ionic radii*? This was because many of the doped elements under consideration were multivalent. In this situation, the oxidation state of the dopant within the LFP structure remained indeterminate. Consequently, since the ionic radius is influenced by the oxidation state, the previously noted uncertainty has rendered it ambiguous which ionic radius should be taken into account.
2. *What was the rationale for selecting differences concerning both Fe and Li*? The purpose of this was to examine if one of the two components of the LFP structure (i.e., Li or Fe) might play a more significant role.

- **Utilizing Pearson correlation for feature selection**

To examine the influence of each input parameter, identify the predominant role of either Fe or Li, improve model efficiency, and minimize redundancy, a Pearson correlation coefficient analysis was conducted. Following the evaluation of the most impactful and significant features, features exhibiting high collinearity were excluded to mitigate the risk of overfitting and redundancy. In this way, this step was undertaken for the following reasons:

- o High collinearity might bias the understanding of feature significance.
- o It minimizes the likelihood of multicollinearity, which can lead to instability during training.
- o It enhances the effectiveness and clarity of the model.

For the purpose of comparison and to identify the impact of eliminating redundant features on the prediction accuracy of the developed machine learning models, the models were trained on both datasets: the complete dataset with all initial input features and the reduced dataset, which was created after the removal of highly correlated features.

- **ML model development and training**

(A) **Gaussian Process Regression (GPR)**

Based on Bayesian inference, GPR is a probabilistic model with uncertain prediction-making. It catches complicated correlations with kernel functions, performs well for small to medium datasets, and offers uncertainty estimations. GPR is prone to overfitting on small datasets; hence, a 10-fold cross-validation (CV) approach was used. The dataset was therefore divided into ten equal sections, and the model was trained on nine folds and validated on the one fold left. This method was conducted ten times, each with a distinct fold serving as the validation set. The average performance throughout all the folds came to define the final model performance. This approach guarantees that every data point is used for training and validation at least once, so a more accurate assessment of model performance would be obtained with less bias than with other strategies including single train-test split.

GPR works based on the assumption of a prior probability distribution for the data being modeled. Afterward, a kernel function defines relationships between data points, and the model learns by optimizing the likelihood of observed data. Finally, predictions are made as the mean value of a probability distribution rather than a single point estimation. In this regard, the uncertainty associated with the prediction is also available, making it straightforward to compare the result obtained by this model at a specific point with that obtained from a different source. This property of GPR was employed in this study to investigate the synergic effects of various combinations of co-dopants, which will be discussed in the consecutive sections.

(B) **Random Forest (RF)**

Random Forest is a method that utilizes an ensemble of multiple decision trees for its learning process. Every tree is developed using a specific portion of the data, and the ultimate prediction is derived by averaging the outcomes from all the trees. This model effectively manages high-dimensional data, mitigates overfitting through the averaging of several models, and demonstrates strong performance with non-linear relationships. A 10-fold CV validation strategy was implemented in this instance as well.

RF operates by randomly dividing the dataset into several subsets through the method of bootstrap sampling. Independent training of decision trees is conducted utilizing various subsets. By employing this method, each tree is developed using a random selection of features, which helps to mitigate overfitting. Ultimately, the predictions are derived by averaging the results from each individual tree.

2.2. Analysis of synergy

After model development, data regarding various co-doped LFP active materials were extracted from the literature. To analyze the possible synergy between co-dopants, first, the anticipated improvement in the LFP's SDC due to each individual dopant was obtained based on

the best ML model developed. Then, by defining synergy as the deviation from the sum of the contribution of individual dopants, the difference between actual values and summed predictions was calculated. This difference was then subjected to another ML analysis, and the relationship between the features corresponding to the heavier dopant and those corresponding to the lighter dopant with that difference was investigated. Finally, to evaluate the study of synergy, a novel co-doped LFP/C active material was fabricated, and its SDC was compared with the analysis predictions.

2.3. Materials

In the conducted research, raw materials with the purity levels specified in Table 1, along with ethanol of 99.9 % purity as a homogenizing solvent, were used during the milling process.

2.4. Synthesis of raw $LiFePO_4$

The schematic illustration of the synthesis procedure is shown in Fig. 1(b). In this manner, Li_2CO_3, $NH_4H_2PO_4$, and $FeC_2O_4{\cdot}2H_2O$ were initially mixed in a stoichiometric ratio of 1:1:1. This mixture, combined with 70 cc of ethanol, was milled using a planetary ball mill for 10 hours at a rotational speed of 400 rpm to achieve homogenization and reduce particle size. The milling process utilized three sizes of steel balls (4 mm, 8 mm, and 9 mm) with a powder-to-ball ratio of 1:20. After drying the slurry in an oven at 60°C for a duration of 24 hours, the resulting powder underwent pre-calcination at 400°C for a duration of 8 hours in a tubular furnace. Meanwhile, an argon atmosphere with a purity of 99.9 % was maintained. The pre-calcined powder underwent a milling process for 2 hours at a rotational speed of 400 rpm to attain a finer and more uniform particle size, utilizing 5 mm zirconia balls during the procedure. As the synthesis temperature can profoundly affect the microstructure and properties of the final materials, samples were calcined at different temperatures of 550°C, 600°C, 650°C, 700°C, and 750°C. This helped the assessment of the impact of temperature and choosing the most appropriate synthesis route. The synthesis was conducted in both powder and tablet formats.

2.5. Synthesis of $LiFePO_4/C$ composite

To produce the $LiFePO_4$/C composite, based on previous studies, Super P carbon was used as the carbon source at 5 % of the weight of $LiFePO_4$. After the first calcination stage, it was added to the raw powder along with a small amount of ethanol using an attrition mill. The powder mixture was dried and calcined at the optimal temperature.

2.6. Synthesis of $LiFe_{(1-X-Y)}Nd_XY_YPO_4/C$ composite

In this stage, based on prior studies, two types of dopants, neodymium oxide and yttrium oxide, were used. The neodymium oxide content was fixed at 0.06, while the yttrium oxide content was selected as 0.02, 0.03, 0.04, 0.07, and 0.08. The dopant oxides were added to the raw materials from the beginning, and the synthesis process followed the same steps as described earlier. The carbon source was introduced after the first calcination stage using an attrition mill. Prior to synthesis, the powder was pressed into tablet form using a manual hydraulic press and then calcined.

Table 1
The compilation of substances utilized in this investigation.

Material name	Chemical Formula	Molar Mass	Purity	Manufacturer
Lithium Carbonate	Li_2CO_3	73.891	99.9 %	Merck
Ammonium Dihydrogen Phosphate	$NH_4H_2PO_4$	115.03	99.9 %	Merck
Iron(II) Oxalate	$FeC_2O_4{\cdot}2H_2O$	143.91	99.9 %	Alpha
Neodymium Oxide	Nd_2O_3	336.48	99 %	MatecK
Yttrium Oxide	Y_2O_3	225.81	99 %	MatecK
Glucose	$C_6H_{12}O_6$	180.156	98 %	Sigma-Aldrich
Carbon (Super P)	C	12.01	99.9 %	MTI Corporation
Polyvinylidene Fluoride	$(C_2H_2F_2)_n$	146.06	99 %	LI-COR

2.7. Characterization and testing

This study involved the characterization of synthesized samples through a range of analytical methods, such as TGA, DTA, SEM, CV, EIS, and XRD. GCD tests were also conducted across several cycles to assess the longevity of the battery.

The TG analysis of the samples was performed utilizing a Netzsch-STA 449 C apparatus, operating within a temperature ranging from 20 to 850 °C, with the rate of heating set at 10 °C/min in an air environment. Furthermore, a comprehensive phase analysis of each sample was conducted employing XRD with a D8 X diffractometer (Bruker, Germany), using Cu-Kα radiation. The scan data were gathered over a 2θ range of 10–70°, employing a step size of 0.013° and a count duration of 6 seconds. The shape of the synthetic compounds was assessed utilizing a JEM-6701F microscope (Jeol, Japan) for SEM analysis and a JEM2100F transmission electron microscopy (Japan) for TEM studies.

The mass loadings of the fabricated cathodes were as follows: for each case, 80 portions of the synthesized cathode powder were mixed with 15 portions of acetylene black and 5 portions of PTFE to form the cathode for the electrochemical measurements. To obtain an integrated cathode material capable of being cut, rolling was employed to form the mixture into a sheet measuring 0.15 mm in thickness. This sheet was then cut into tablets. The assembly of half-cells involved a) Li as the anode, b) a mixture of 1 M $LiPF_6$ with ethylene carbonate and dimethyl carbonate (having equal volume ratios) as the electrolyte, and c) Celgard 2400 microporous membrane as the separator. This process took place in a glove box filled with nitrogen, maintaining a relative humidity of less than 3 %. The cells underwent charging and discharging processes within a voltage range of 2.5–4.5 V in relation to the Li/Li^+ electrode at ambient temperature. The CV and EIS tests were performed utilizing a CHI 600 A electrochemical analyzer device. The CV profiles for the investigated cells were documented across a 2.5–4.3 V potential range, utilizing a scan rate of 0.05 mV/s. The EIS measurements were conducted over the range of frequency from 10 kHz to 10 mHz, utilizing an AC voltage of 5 mV. The experiments involving CV and EIS were conducted using a three-electrode system, with lithium foils serving as the counter and reference electrodes.

3. Result and discussion

3.1. The Pearson correlation coefficient matrix

Fig. 2 depicts the result of collinearity analysis in terms of the Pearson correlation coefficient matrix. Several aspects can be identified from this figure, including:

1) As it was speculated, there are high levels of collinearity between $\Delta r_{Fe\_ion} - \Delta r_{Fe\_atom}$, $\Delta r_{Fe\_ion} - \Delta r_{Li\_atom}$, $\Delta r_{Fe\_ion} - \Delta r_{Li\_atom}$, $\Delta r_{Li\_ion} - \Delta r_{Li\_atom}$, and $\Delta r_{Fe\_atom} - \Delta r_{Li\_atom}$. However, it can be seen that the correlation in the $\Delta r_{Li\_atom} - SDC$ and $\Delta r_{Fe\_atom} - SDC$ sets is more than in the $\Delta r_{Li\_ion} - SDC$ and $\Delta r_{Fe\_ion} - SDC$ sets. As previously discussed, given the uncertainty in the proper selection of ionic radii (due to vagueness of the exact oxidation state of the dopant), these findings suggest that it would be possible to employ atomic radius to predict the efficiency of a dopant in increasing the SDC of LFP. Hence, this parameter is not only more certain but also more effective in predicting the enhanced SDC of a doped LFP.

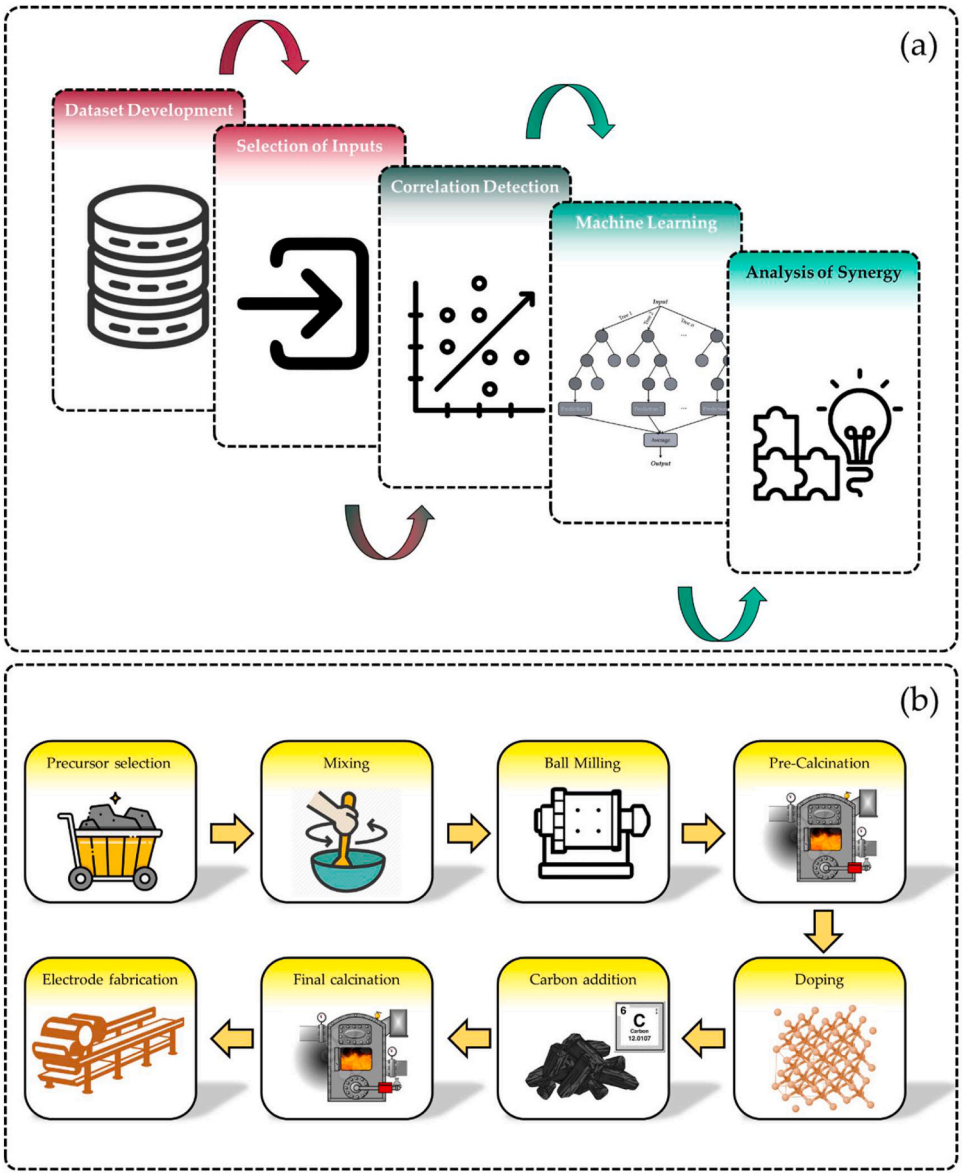

Fig. 1. Schematic overview of (a) the ML employed to detect and analyze possible synergic effects between co-dopants, and (b) the synthesis procedure adopted.

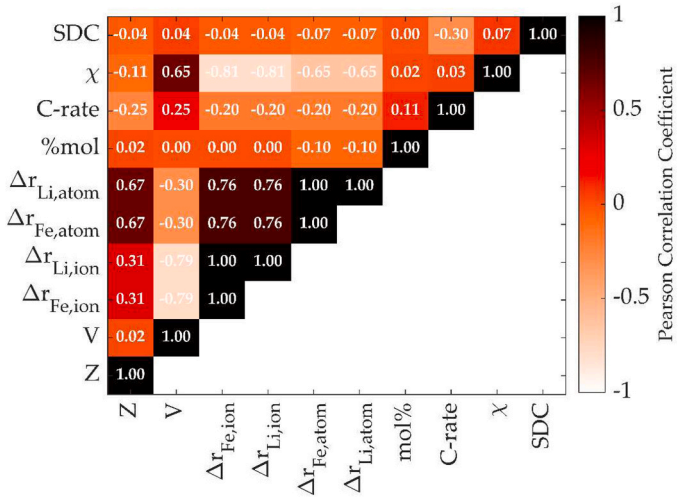

Fig. 2. The Pearson correlation coefficient matrix.

2) No predominant effect of Li or Fe was observed; therefore, these two constituents play the same role.
3) Based on point 1 and point 2, in the rest of the analysis, Δr_{Li_atom} was only considered, and Δr_{Fe_atom}, Δr_{Fe_ion}, and Δr_{Li_ion} were neglected. This omission also vanished the collinearity observable in $V - \Delta r_{Fe\_ion}$, $V - \Delta r_{Li\_ion}$, $\chi - \Delta r_{Fe\_ion}$, and $\chi - \Delta r_{Li\_ion}$ sets.

3.2. ML models' predictions and versatilities

Fig. 3(a) and (b) depict normalized target values vs. each model's predictions. In these figures, scheme 1 corresponds to the model trained on the whole dataset, and scheme 2 corresponds to the model trained on the dataset with the reduced features. As it can be seen, the strategy to shrink the dataset had been successful in improving the accuracy of the model, yet to a limited degree. Nevertheless, the best model was GPR—Scheme 2 in the sense that it yielded an R^2 value of ~0.85 and was employed in the rest of the study to predict the effect of a dopant on the SDC of LFP/C obtained under various C-rates. In these figures, the entire range is divided into three sections, namely low accuracy, medium accuracy, and high accuracy regions. However, regardless of the model type or the scheme, it can be seen that the low accuracy region

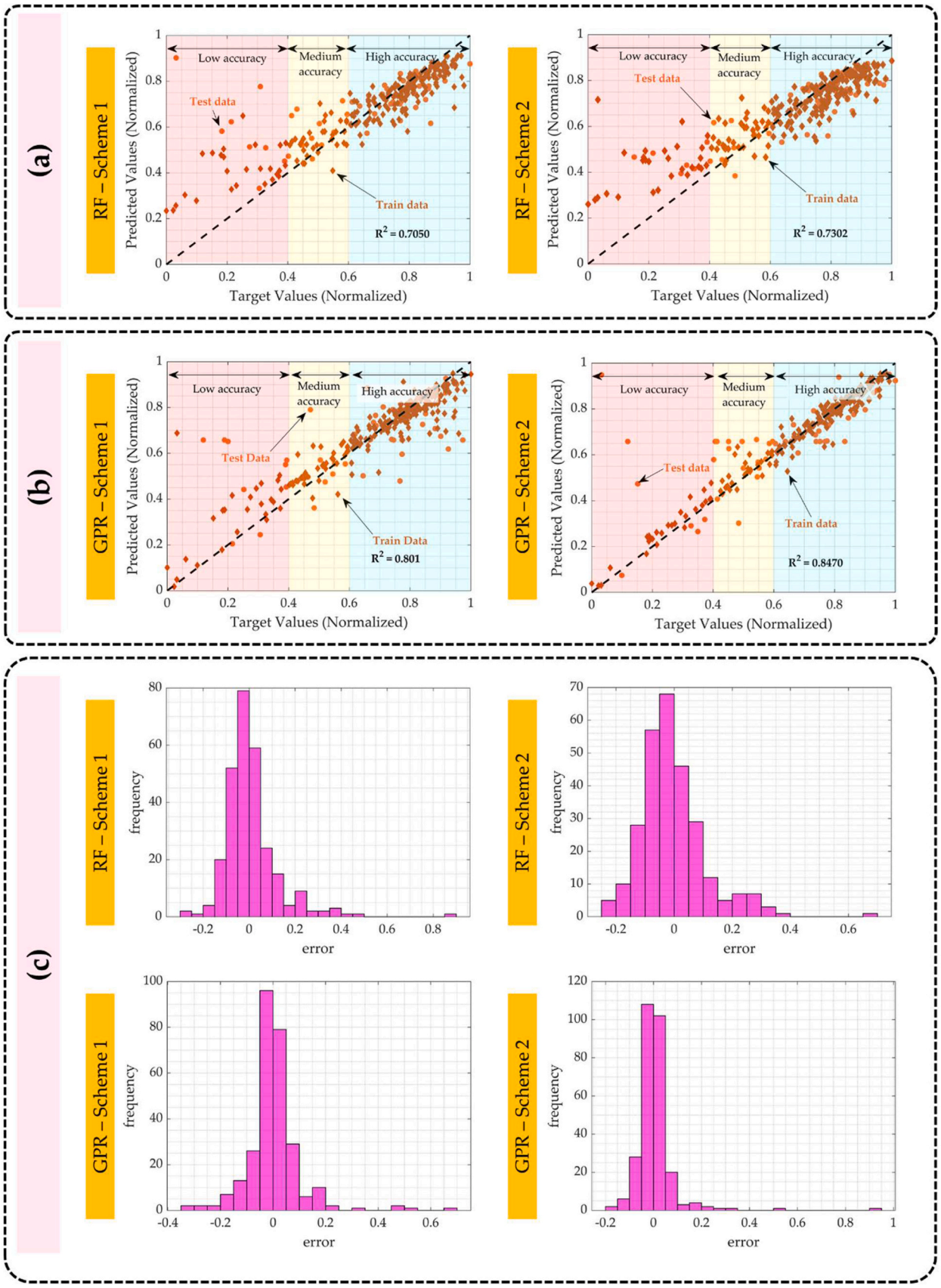

Fig. 3. The efficiency of (a) RF, and (b) GPR model in predicting normalized SDC values, and (c) the statistics of errors associated with each model.

corresponds to the normalized SDCs of less than 0.4, roughly equal to 110 mAh/gr. This observation is most likely due to the imbalance in the data distribution. That is, on one hand, there is plenty of data in the high SDC domain, helping the process of model training and reducing the error in this region. On the other hand, the number of data points in the low accuracy region is more scarce, which makes it challenging for an ML model to learn the relationships between input features and the output well. Hence, it is not surprising to see wider scattered predictions in this region. Fig. 3(c) illustrates the statistics of the errors (i.e., residuals) associated with each model. As can be seen, in each case, this parameter almost follows a normal distribution with its mean centered around 0. By moving from RF—Scheme 1 toward GPR—Scheme 2, error values tighten around the mean, in accordance with the increase in R^2.

The RF—Scheme 2 outcome is presented in Fig. 4, where the variation of normalized SDC with each pair of input variables is shown, keeping other normalized input features at 0.6. As can be seen, these figures are in well accordance with the Pearson correlation coefficient matrix. For instance, the fact that increasing C-rate decreases the SDC is well captured by each figure where C-rate is one of the axes. As another example, at a certain concentration, increasing $\Delta r_{Li,atom}$ increases the SDC up to a certain point, and further increases in this parameter yield a decrement in the SDC. This phenomenon can be observed in many previous works, and also in this work, and is mainly due to the formation of secondary phases or an excessive distortion of the LFP lattice, making this structure unstable during the operation of the battery.

3.3. Determination of calcination temperature

Fig. 5 presents the TGA-DTA analysis of the powder mixture of raw materials. Based on this figure, several phenomena can be identified. The evaporation of moisture and other volatile contaminations absorbed by the sample results in a primary weight loss of up to ~110°C. However, three distinct weight loss regions are observed thereafter. In the region between ~110°C and ~200°C, the weight loss observed is attributed to the dehydration of the $FeC_2O_4{\cdot}2H_2O$ compound, as described by Eq. (1). This is consistent with the exothermic reaction observed at ~150°C on the DTA curve.

$$FeC_2O_4 \bullet 2H_2O \rightarrow FeC_2O_4 + 2H_2O \quad (1)$$

The thermal decomposition of $NH_4H_2PO_4$ and FeC_2O_4 accounts for the subsequent weight loss, occurring between ~200°C and ~400°C, as described by Eqs. (2) to (3). Based on the peaks observed in the DTA curve, these decomposition reactions occur as two exothermic events at ~230°C and ~287°C. The decomposition during this stage is critically important; incomplete decomposition of FeC_2O_4 contributes to undesirable Fe_2O_3 phase formation, as described by Eq. (4). Moreover, obtaining a high-purity $LiFePO_4$ phase requires a stoichiometric amount of the FeO phase.

$$NH_4H_2PO_4 \rightarrow NH_3 + H_3PO_4 \quad (2)$$

$$FeC_2O_4 \rightarrow FeO + CO_2 + CO \quad (3)$$

$$2FeC_2O_4 \rightarrow Fe_2O_3 + CO_2 + 3CO \quad (4)$$

The third weight loss region corresponds to a slight weight change in the temperature range of 400°C to 500°C, which indicates the initiation of $LiFePO_4$ phase synthesis at temperatures above 400°C. Furthermore, based on the DTA curve, the solid-state reaction and crystallization of the $LiFePO_4$ phase occur at 506°C.

Based on the analysis of Fig. 5 and previous studies, a temperature of 400°C was selected for the initial calcination stage to decompose the compounds and eliminate volatile substances. However, prior to the carbonization step, to determine the optimal temperature and microstructure, the samples underwent final calcination at various temperatures (650°C, 700°C, 750°C, 800°C, and 850°C) for 14 hours to synthesize the $LiFePO_4$ phase.

3.4. XRD study results

Fig. 6(a) displays the reference pattern of LFP. Based on the comparison of the XRD pattern of LFP and LFP/C samples synthesized at various temperatures, presented through Fig. 6(b) and (c), respectively, with this reference pattern, it can be concluded that the synthesis was successful. The fact that no additional primary peaks are observed indicates the absence of impurity phases in the synthesized specimens, which can alter the active material's performance to a great amount. Overall, from the perspective of the evolution of the structure after calcination of specimens at different temperatures, it can be seen that by increasing the temperature from 550°C, the intensity of peaks increases and they become narrower. This can be attributed to the material retaining its stable crystalline structure, which becomes more profound as temperature increases. However, beyond 650°C, the peaks' intensities start to fall again. This can be due to the excessive evaporation of volatile species, such as Li, from the structure as temperature increases beyond some optimum point, located near 650°C. In this manner, it seems that 650°C was the best synthesis temperature despite the fact that the decrease in the peaks' intensities was not considerably significant. Yet, generally, it is more desirable to synthesize cathode-active materials at as low as possible temperatures. This is due to the fact that the lower the temperature the lower the fabrication costs, and process complexities such as volatile elements loss.

Moreover, the effect of the carbon layer, applied on the surface of particles, on the structural evolution of specimens during the synthesis was also investigated. This was crucial as the application of a carbon layer on the surface of specimens was an inseparable part of the synthesis of LFP/C and doped specimens. Fig. 6(c) depicts the XRD patterns corresponding to the LFP/C specimens. As can be seen, the same trend as that of Fig. 6(b), increasing the crystallinity and stability of the structure up to 650°C followed by a decrease in the peaks' intensities at higher temperatures, is observable here too. In this way, it is rational to conclude that the carbon coating did not affect the synthesis of the specimens.

Fig. 6(d) illustrates the XRD patterns of samples containing 0.02, 0.03, 0.04, 0.07, and 0.08 yttrium and 0.06 neodymium oxide synthesized at 650°C. Based on the results shown in this figure, it can be concluded that all samples lack any additional peaks corresponding to impurity phases. In other words, the added neodymium and yttrium oxides are within the permissible range, and have fully integrated into the LFP lattice by reacting with the raw materials, replacing cations without altering the lattice structure.

Based on these observations, it can be deduced that the temperature of 650°C and the synthesis duration of 14 hours are suitable conditions for the reactions to occur. Furthermore, as observed in the patterns, the addition of dopant oxides to the composition causes slight peak shifts. These shifts are due to the replacement of Fe^{2+} ions (ionic radius of 78 pm) in the lattice with Y^{3+} and Nd^{3+} ions, which have larger ionic radii of 90 pm and 99.5 pm, respectively, resulting in an increased lattice parameter.

3.5. Examination of the undoped sample

Fig. 7(a) shows the SEM images of milled powders before and after the synthesis of LFP at 650°C. It can be seen that, before synthesis, the particles have an irregular and elongated shape. However, after calcination at 650°C, the particles transition into a semi-spherical shape. To examine the elements present in the composition and evaluate their distribution in the synthesized samples, EDS analysis was also conducted. As shown in Fig. 7(b), the distribution of iron, phosphorus, and oxygen is uniform in the $LiFePO_4$ composition synthesized at 650°C.

3.6. Morphological analysis of samples

As the geometrical and statistical features of the cathode active

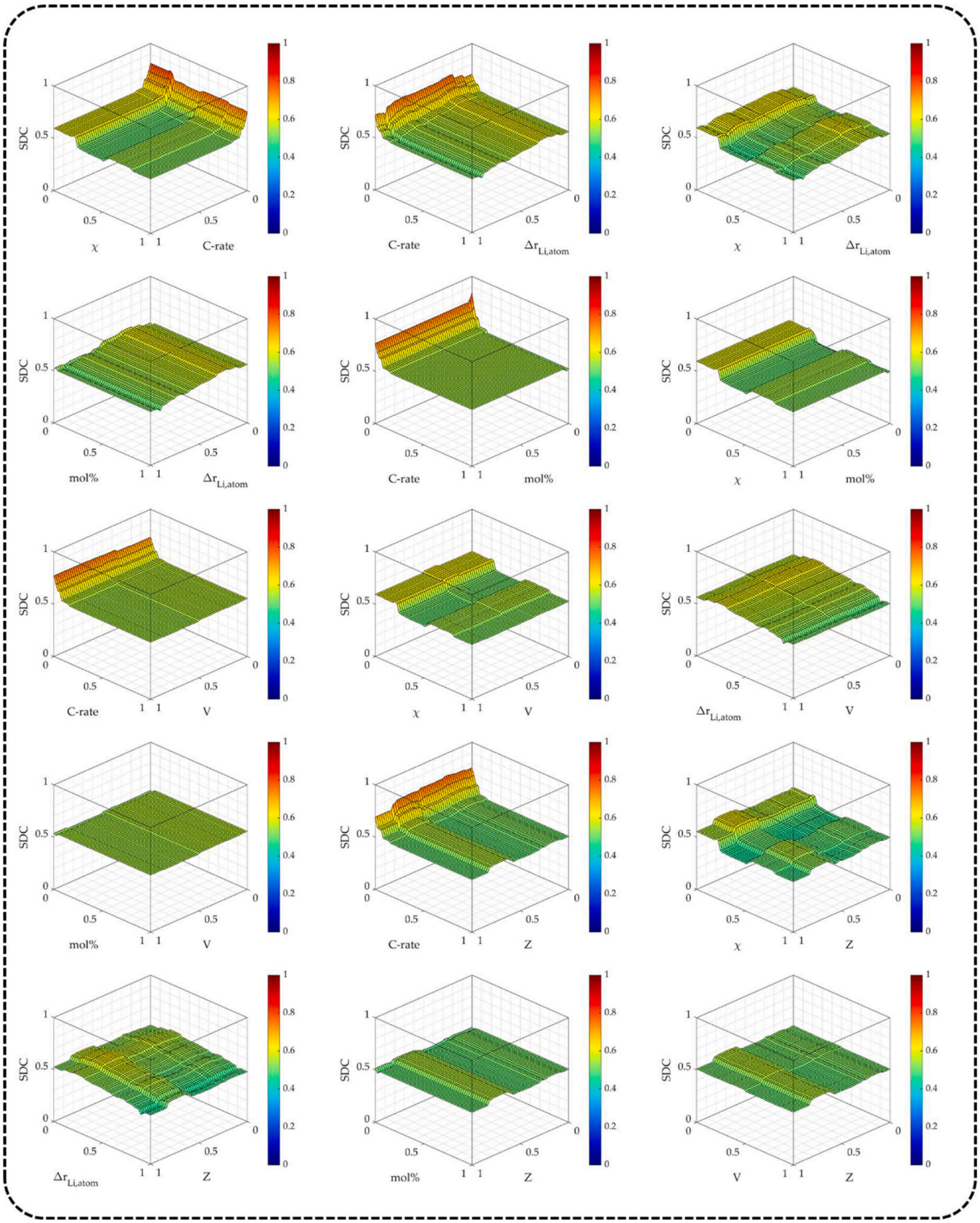

Fig. 4. 3D plots of the predictions of the RF – Scheme 2 model regarding the binary effect of input features on the normalized SDC.

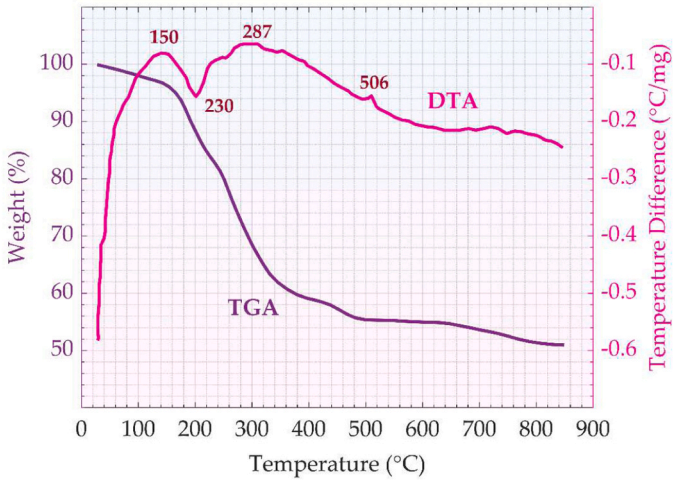

Fig. 5. TGA/DTA thermograms of the obtained powder mixture.

material have a significant effect on the electrochemical behavior, these parameters are investigated in Fig. 8. In Fig. 8(a), the SEM image of the synthesized samples, namely pristine LFP, LFP/C, LFP-$Y_{0.03}Nd_{0.06}$/C, LFP-$Y_{0.04}Nd_{0.06}$/C, and LFP-$Y_{0.07}Nd_{0.06}$/C are presented. Fig. 8(b) demonstrates the corresponding particle size distribution analysis for each sample. Moreover, a log-normal distribution with the definition given by Eq. (5) is fitted to each case, and the results in terms of mean, standard deviation, and goodness-of-fit are reported in Table 2. To calculate the goodness-of-fit, the cost function was chosen to be mean square error with its definition given by Eq. (6).

$$f(x;\mu\&\sigma) = \frac{1}{x\sigma\sqrt{2\pi}}\exp\left(-\frac{(\ln(x)-\mu)^2}{2\sigma^2}\right) \tag{5}$$

$$MSE = \frac{\sum_{i=1}^{N}\left(F_{empirical}(x) - F_{fitted}(x)\right)^2}{N} \tag{6}$$

In Eq. (7), $F_{empirical}(x)$ is the empirical cumulative distribution function, and in Eq. (8), $F_{fitted}(x)$ is the fitted one. These two functions can be defined as:

$$F_{empirical}(x) = \frac{Number\ of\ data\ points \le x}{Total\ number\ of\ data\ points} \tag{7}$$

$$F_{fitted}(x) = \frac{1}{2}\left[1 + erf\left(\frac{\ln(x)-\mu}{\sigma\sqrt{2}}\right)\right] \tag{8}$$

As Table 2 suggests, the application of carbon coating yielded a lower particle size compared to the uncoated sample; simultaneously, the value of the standard deviation was also decreased. The latter means that this strategy also resulted in a narrower distribution (particles with almost identical size). It is a well-established rule that these characteristics contribute to the enhanced electrochemical properties. Moreover, the addition of doping elements caused a further decrease in the mean size while keeping the standard deviation almost intact. Yet, for the case of Y0.07, it can be seen that both the mean value and standard deviation increased significantly. As a matter of fact, the high values of MSE indicate that the distribution of particles, in this case, does not follow the normal distribution; rather, it's of a multi-modal form.

It is evident from Fig. 8(b) that for the case of the LFP sample, the particle size distribution ranges approximately between 300 and 1000 nm. However, with the addition of carbon as a coating to the LFP particles, a separating layer is formed by the carbon network settled on the particles, hindering particle growth and agglomeration at elevated temperatures. This results in a reduction of the particle size distribution range to nearly half of the previous range (approximately 50–450 nm),

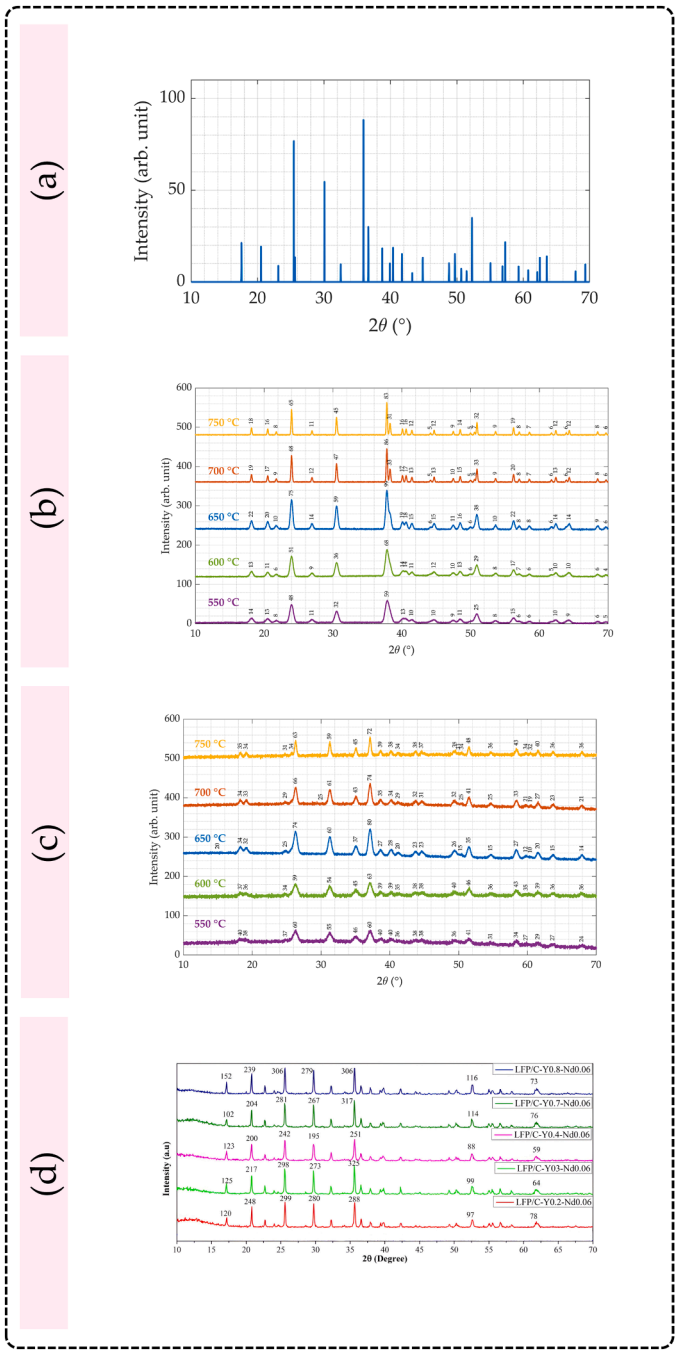

Fig. 6. (a) the reference XRD pattern of LFP, (b) XRD patterns of LFP samples synthesized at various temperatures, (c) XRD patterns of LFP/C samples synthesized at various temperatures, and (d) XRD patterns of LFP/C specimens containing different amounts of Y synthesized at 650°C.

as clearly shown in the case of the LFP/C sample. In this regard, the addition of carbon reduced the average particle diameter from 431 nm to 153 nm. Moreover, the SEM images and particle size distribution diagrams of doped-LFP/C samples show that the addition of neodymium and yttrium reduces the particle size compared to the LFP sample. Additionally, the addition of yttrium further reduces the particle size up to 0.04. However, for yttrium contents exceeding that value, the particle size distribution becomes much broader (ranging from 400 to 1400 nm), leading to an increase in the average particle size to 793 nm.

This reduction can be attributed to the incorporation of neodymium, which replaces iron, and to a very small extent, lithium, causing

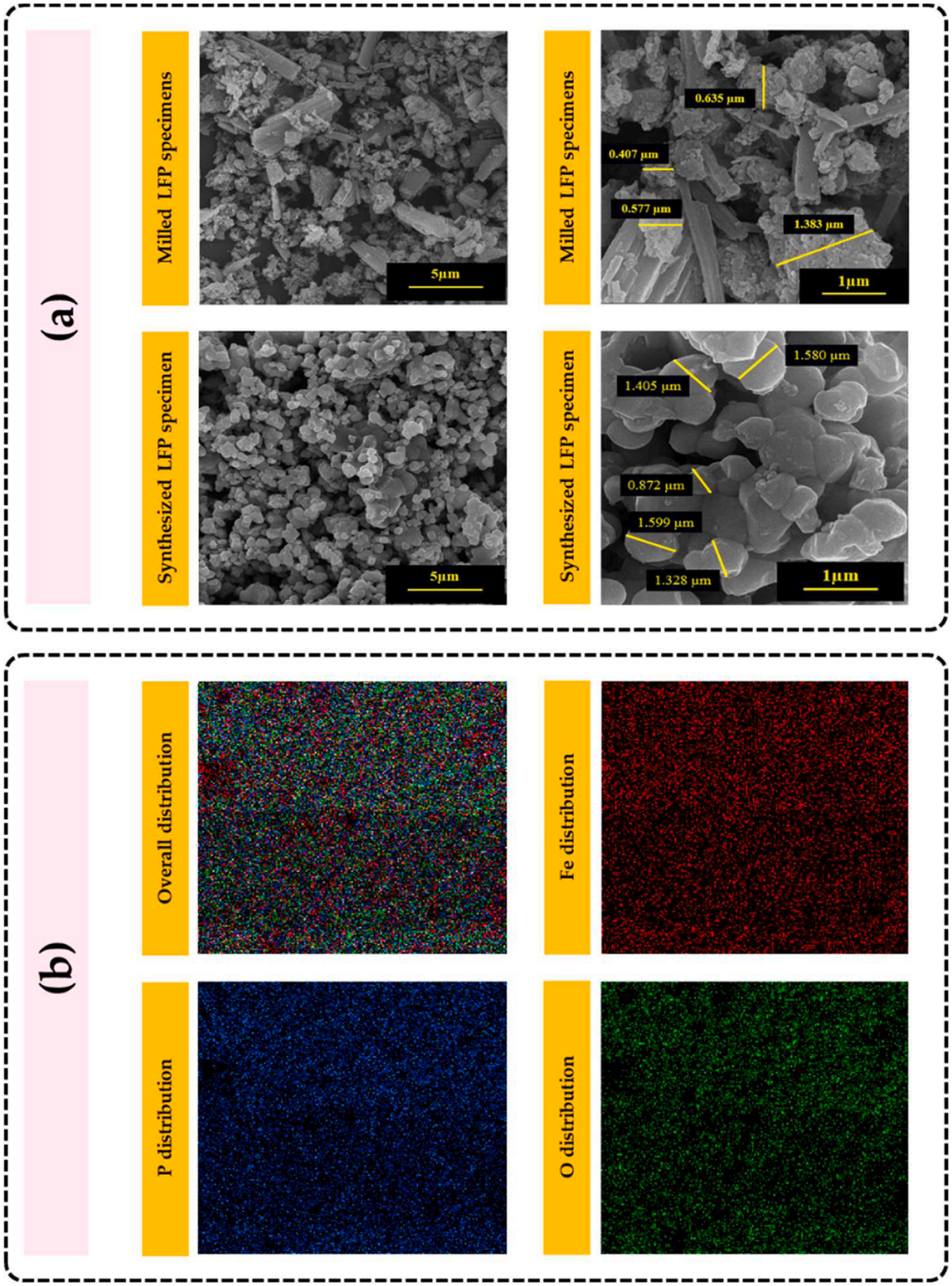

Fig. 7. SEM moicrographs of (a) milled and calcined (at 650°C) LFP specimens, and (b) Results of EDS analysis and distribution of Fe, P, and O within the synthesized $LiFePO_4$ specimen.

distortions in the LFP crystal lattice and ultimately leading to smaller particle sizes. Such a trend in the variation of the mean particle size with the addition of a dopant has been observed in many previous studies and is attributed to several factors. These include the effect of dopant on surface energy, grain boundary mobility, lattice distortion, and probably other phenomena [73–77].

Fig. 9 shows the carbon layer applied on the surface of the synthesized powders. It can be seen that the applied layer has almost a uniform thickness, which is promising for the electrochemical performance of the cathode active material. Fig. 10 illustrates the TEM micrographs of the pristine LFP and doped structures. As can be seen, TEM micrographs are in accordance with the SEM analysis from the perspective of particle size. Moreover, the discrepancy between the size of particles is evident in the case of the specimen doped with 0.07 Y.

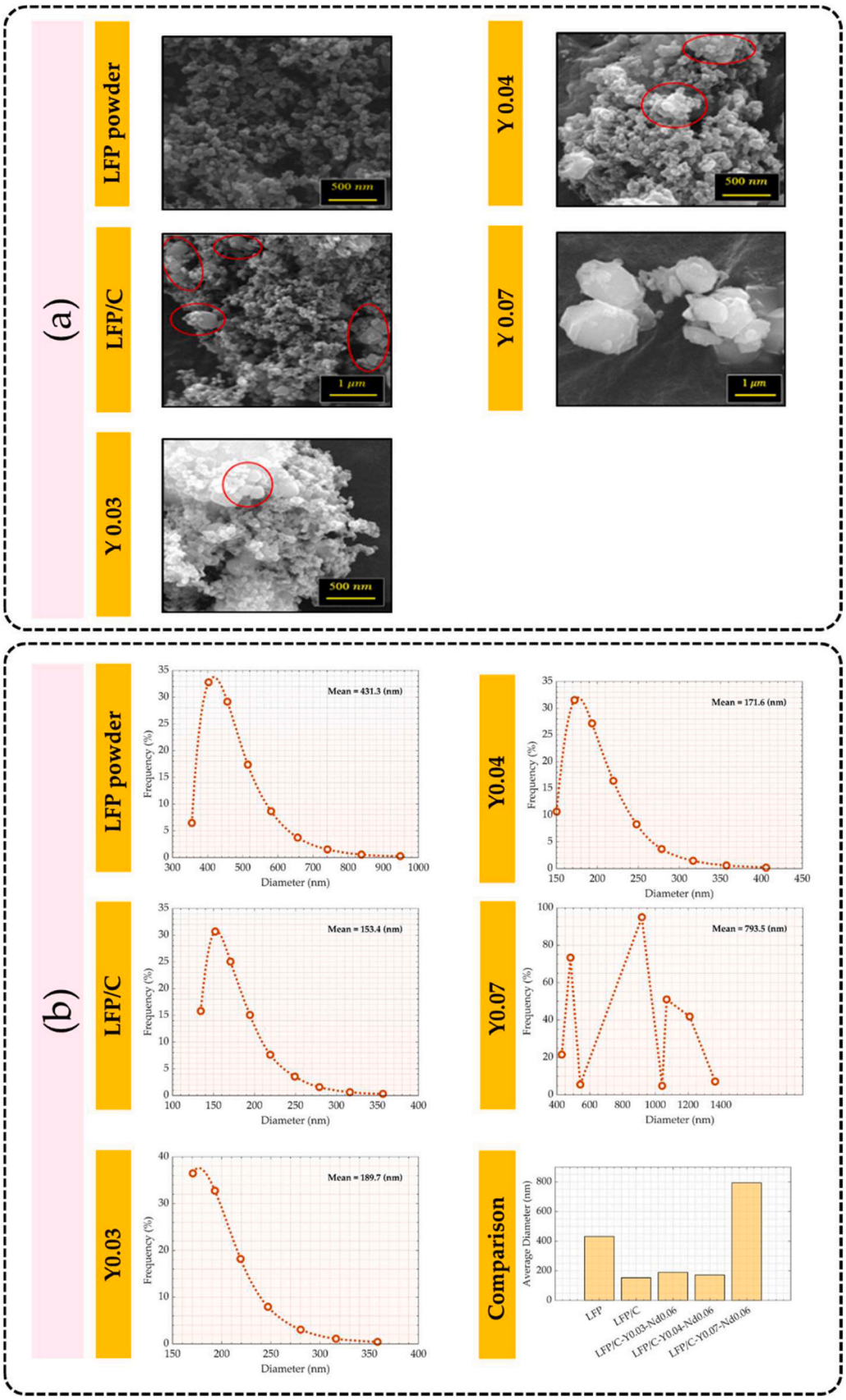

Fig. 8. (a) Particle size distribution and (b) corresponding SEM images of specimens with different chemical compositions, all synthesized at 650°C.

Table 2
The variation of the mean size, standard deviation, and MSE for different specimens.

Sample	μ	σ	MSE
LFP	431.3	79.1	0.0866
LFP/C	153.4	31.6	0.0857
Y0.03	189.7	29.3	0.1060
Y0.04	171.6	34.6	0.0824
Y0.07	793.5	337	0.2508

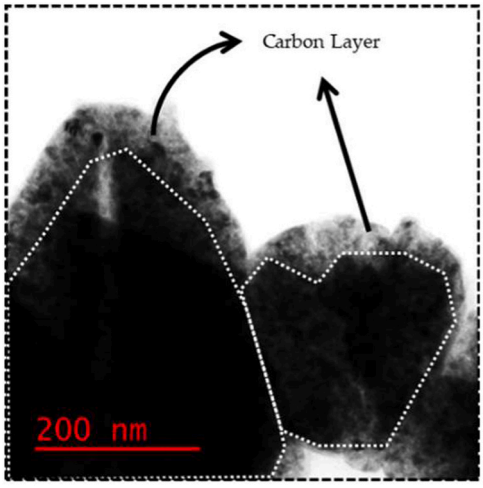

Fig. 9. Applied carbon layer on the surface of synthesized powder particles.

Additionally, HRTEM analysis shows a consistent lattice expansion as a result of the addition of dopants. Y and Nd, with atomic radii of 180 pm and 185 pm, respectively, can replace lithium (145 pm) and iron (140 pm) in the $LiFePO_4$ lattice. This substitution causes distortions and opens up the lattice structure. Additionally, Y^{3+} and Nd^{3+} ions, when substituting Fe^{2+} in the lattice, create electronic defects with a charge of + 1. These factors facilitate lithium-ion diffusion and enhance the material's electrical conductivity. In this manner, it is expected that such increased lattice volume, which primarily affects diffusion, along with the generated electronic defects, manifest themselves in the electrochemical performance of the material.

3.7. Analysis of cyclic voltammetry curves

The CV curve for $LiFePO_4$ (Fig. 11) shows an anodic peak corresponding to the oxidation reaction of Fe^{2+} to Fe^{3+} in the $FePO_4$ compound and a cathodic peak corresponding to the reduction reaction of Fe^{3+} to Fe^{2+} in the $LiFePO_4$ compound. However, it must be remembered that due to the charge neutrality constraint, this Redox reaction is coupled with the insertion/removal of Li into the $LiFePO_4$ structure. Moreover, these oxidation/reduction reactions are indicators of successful electron transfer.

Fig. 11(a) illustrates the CV curve of the powder LFP sample. The figure illustrates anodic peaks occurring at approximately 3.5–3.6 V and cathodic peaks at about 3.25–3.3 V for the initial and fourth cycles, respectively. The voltage difference between the anodic and cathodic peaks across the first and fourth cycles relates to the development of the cathode–electrolyte interphase (CEI) layer on the surface of the cathode. This formation plays a significant role in attaining relative stability during the insertion and removal processes of Li-ion after the second cycle. The analysis of this stability can be conducted by examining both the peak current intensity and the corresponding voltage at which these peaks manifest.

In this regard, the current magnitude decreases from the first to the fourth cycle, indicating a reduction in the cathode capacity during multiple charge/discharge cycles. The higher peak current in the first cycle can be attributed to the energy consumption required for the formation of the CEI layer. Consequently, in the first cycle, a portion of the capacity is irreversibly consumed for the formation of this layer. The amount of this irreversible capacity consumption decreases significantly for subsequent cycles as the CEI layer stabilizes. Therefore, the relative reduction in peak current intensity from the second to the fourth cycle can be interpreted as a decrease in the cathode's charge and discharge capacity.

Additionally, in the first cycle, the curve shows discontinuity around 2.5 V. The anodic and cathodic peak voltages exhibit a wide range, which indicates strong internal polarization. This discontinuity at approximately 2.5 V in the first cycle can be attributed to the formation of the CEI layer, leading to uneven electrochemical processes. The strong internal polarization observed further highlights the resistance associated with the initial formation of the CEI layer and the stabilization of lithium-ion pathways [78–81].

Fig. 11(a) also illustrates the CV curve of the LFP tablet sample. As observed, this diagram demonstrates better performance compared to the powder sample in several aspects:

1. The peak current intensities of both anodic and cathodic peaks are higher in the pelletized sample, indicating greater capacity and faster lithium-ion diffusion during insertion and removal processes compared to the powdered sample.
2. The stability of the peaks, particularly during the cathode discharge process, is a positive characteristic of this sample. This stability corresponds to the formation of a more desirable CEI layer, which contributes to capacity retention over successive cycles.

Fig. 11(b) presents the CV curves of composite LFP/C samples with different doping levels. For the case of the undoped LFP/C sample, during the charge/discharge process in cycles 2 and 3, the material did not exhibit stable ionic conductivity. Due to the inability to transfer and release lithium ions effectively, the charge/discharge process was not successfully completed in these cycles. However, the material recovered in the fourth cycle, successfully completing the cycle.

By comparing cycles 1 and 4, it can be observed that the current density increases from cycle 1 to cycle 4, indicating faster lithium-ion diffusion. Additionally, the voltage range of the peaks narrows from cycle 1 to cycle 4, meaning the anodic peak voltage decreases while the cathodic peak voltage increases. This reduction in the voltage difference between the two peaks can be attributed to reduced polarization.

Fig. 11(c) compares the first and fourth cycles of cyclic voltammetry for various samples. As observed in the figure, with the addition of carbon and dopant oxides to the composition, along with optimizing their amounts, the anodic and cathodic peaks become closer to each other. This convergence confirms improved reversibility (defined by Eq. (9)) of the redox reactions in the samples. This parameter is compared for different specimens in Table 3 and it can be seen that the sample with 0.04 Y content (LFP/C-$Y_{0.04}$-$Nd_{0.06}$) exhibits the best behavior.

$$Reversibility(\%) = \frac{Cathod\ Voltage_{i^{th}cycle}}{Anode\ Voltage_{i^{th}cycle}} \times 100 \quad (9)$$

In fact, with the addition of dopant elements at optimal levels (i.e. ~0.04), the ionic conduction network expands, and the creation of electronic defects in the structure enhances electrical conductivity. As a result, the reaction kinetics within the structure improve, enabling the material to respond rapidly to charge/discharge processes and mitigate capacity loss during these processes. This behavior ultimately leads to improved reversibility.

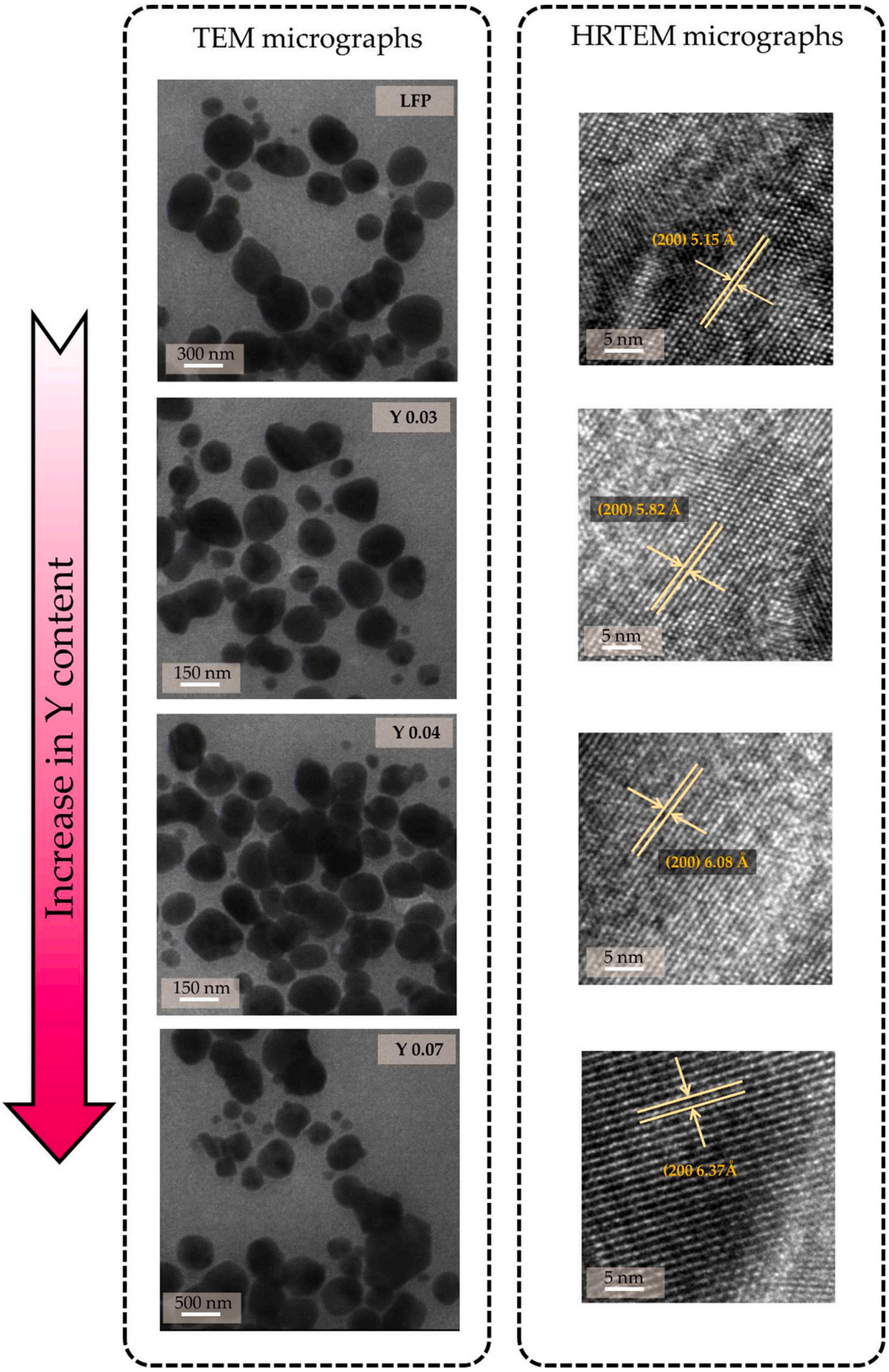

Fig. 10. Effect of the addition of Y on the LFP lattice expansion.

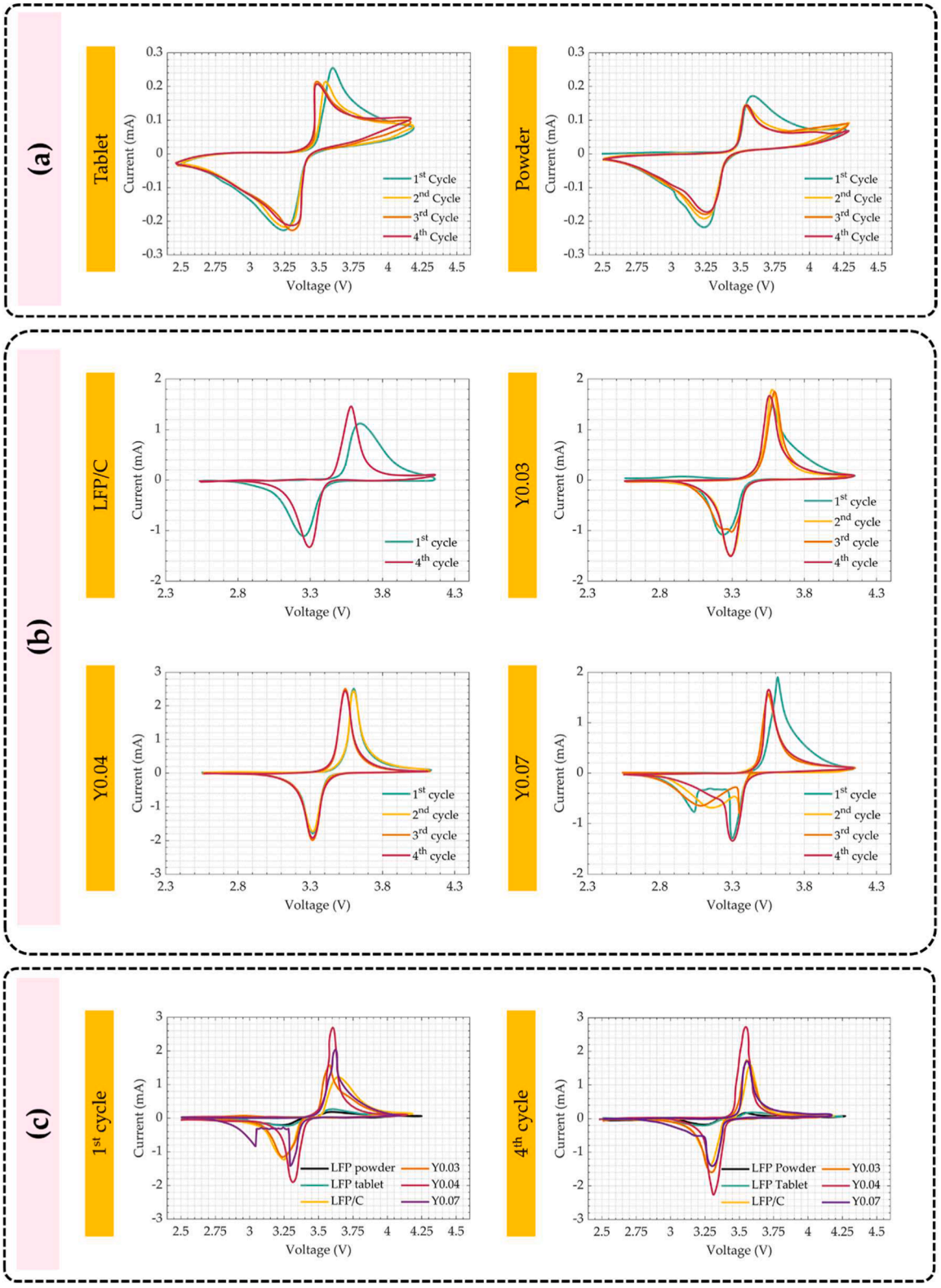

Fig. 11. (a) CV curves of LFP powder and LFP tablet samples, (b) CV curves of LFP/C, LFP/C-$Y_{0.03}$-$Nd_{0.06}$ (denoted by $Y_{0.03}$), LFP/C-$Y_{0.04}$-$Nd_{0.06}$ (denoted by $Y_{0.04}$), and LFP/C-$Y_{0.07}$-$Nd_{0.06}$ (denoted by $Y_{0.07}$), and (c) Comparison of the CV curves corresponding to the first and fourth cycles of the materials investigated in this study.

3.8. Analysis of discharge capacity

Fig. 12(a) illustrates the variation in discharge capacities of different $LiFePO_4$/C samples during the formation stage. In this stage, the electrolyte is simultaneously exposed to electrons present on the electrode surfaces under a specific voltage range, ultimately leading to the formation of an interfacial layer on the surface of both the anode and cathode.

During charging, the electrolyte decomposes and deposits on the anode surface through reductive reactions at low potentials, and on the

Table 3
Comparison of the reversibility of different specimens in their 1st and 4th cycles.

Sample		Cathode Voltage (V)	Anode Voltage (V)	Reversibility (%)
Raw LFP (Powder)	1st cycle	3.23	3.6	89
	4th cycle	3.26	3.53	92
Raw LFP (Tablet)	1st cycle	3.24	3.6	90
	4th cycle	3.26	3.55	91
LFP/C	1st cycle	3.25	3.64	89
	4th cycle	3.3	3.57	92
LFP/C-$Y_{0.03}$-$Nd_{0.06}$	1st cycle	3.24	3.57	90
	4th cycle	3.28	3.56	92
LFP/C-$Y_{0.07}$-$Nd_{0.06}$	1st cycle	—	—	—
	4th cycle	3.3	3.55	92
LFP/C-$Y_{0.04}$-$Nd_{0.06}$	1st cycle	3.24	3.6	91
	4th cycle	3.3	3.54	93

cathode surface through oxidative reactions at high potentials. The largest amount of interfacial layers is typically formed during the first charge/discharge cycle, as no interfacial layers have yet been established on the anode and cathode surfaces to electrically insulate the electrodes from the electrolyte. Consequently, the most significant irreversible capacity loss occurs during the first charge/discharge cycle. This capacity loss is significantly reduced from the second and third cycles onward.

If a significant interfacial layer is not formed during the first cycle, subsequent cycles will result in only minimal interfacial layer formation. This occurs because the weak initial layer prevents the electrolyte from reaching the electrode surface and inhibits electron transfer between the two. In fact, irreversible capacity loss varies depending on factors such as particle surface area, operating conditions, and more.

As shown in Fig. 12(a), the discharge capacity for the raw LFP sample synthesized as a powder is initially low, measuring approximately 110 mAh/g in the first cycle. This indicates poor electrical and ionic conductivity in the composition. This issue is partially addressed by pelletizing the powder before synthesis (as in the Bare LFP Tablet sample), improving the discharge capacity to 120.03 mAh/g by the third discharge cycle.

For the LFP/C sample, the addition of Super P carbon as a particle coating significantly improves cathode performance, enhancing the discharge capacity to 133.2 mAh/g and 126.7 mAh/g in the first and third cycles, respectively. This capacity improvement is attributed to increased electrical conductivity and enhanced particle surface area due to the carbon coating on the $LiFePO_4$ particles. Carbon prevents particles

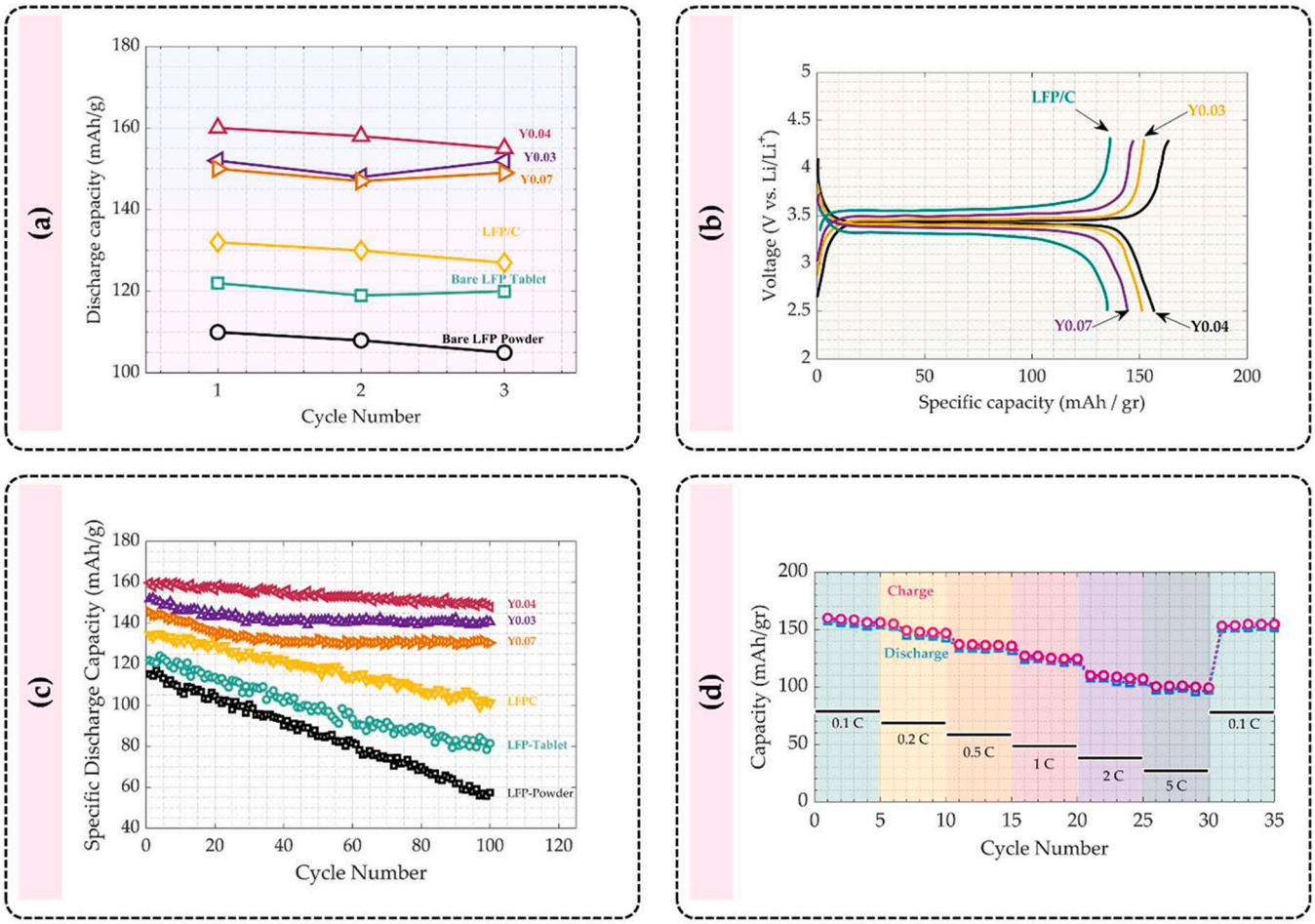

Fig. 12. (a) Variation of discharge capacity during the formation cycles for various cathode materials synthesized in this study, (b) galvanostatic charge/discharge curves of the synthesized cathode active materials obtained at 0.1 C, (c) cycling stability curves of different specimens at 0.5 C and (d) rate capacity of $LiFe_{0.9}Y_{0.04}Nd_{0.06}PO_4/C$.

from adhering to one another, and multiple smaller carbon particles attach to a single LFP particle, effectively increasing the chargeable surface area on the particles.

Based on the data illustrated in Fig. 12(b), which represents the galvanostatic charge/discharge capacity of synthesized materials, it can be concluded that the lattice structure in the sample doped with 0.03 yttrium (Y0.03) is more open compared to the Bare and Tablet samples. This allows lithium-ion diffusion within the lattice to occur more easily during charge/discharge processes. Moreover, the sample doped with 0.04 yttrium (Y0.04) demonstrates even better electrical and ionic conductivity than the Y0.03 sample, resulting in improved charge/discharge capacity. However, excessive yttrium in the lattice (0.07) leads to severe distortions and probably blockage of lithium-ion pathways. This reduces ionic conductivity compared to the sample doped with 0.04 yttrium (Y0.04), which has a nearly optimal amount of yttrium. Table 4 presents the discharge capacities of different samples. As previously mentioned, the Y0.04 sample exhibits the highest discharge capacity, which is compared in Table 5 with several LFP/C-based cathode materials synthesized and tested previously by other researchers.

3.9. Analysis of cycling stability

The cycling performance was evaluated using the discharge capacity over 50 cycles at a charge/discharge rate of 0.5 C. As shown in Fig. 12(c), the raw LFP samples exhibit good stability after 50 discharge cycles. However, with the addition of carbon and dopant elements, the discharge capacity and stability improves, indicated by lowered slope over various cycles.

Upon closer examination of Fig. 12(c), as suggested by the TEM and HRTEM analysis, in the samples doped with 0.07 yttrium (Y0.07) and 0.03 yttrium (Y0.03), the addition of guest elements to the lattice and the resulting lattice expansion improve the discharge capacity compared to the raw LFP and LFP/C samples. However, again, it can be observed that the discharge capacities of samples with the lower and higher Y-content compared to the optimal value, remain lower than that of the sample doped with 0.04 yttrium (Y0.04).

This lower capacity in the Y0.07 sample is attributed to significant lattice distortions caused by the excessive presence of guest atoms in the LFP lattice. With each charge/discharge cycle, some lithium diffusion pathways become temporarily or permanently blocked, preventing lithium-ion movement. On the other hand, the Y0.03 sample has fewer guest atoms and fewer ionic and electronic defects, resulting in less lithium diffusion and weaker electrical conductivity compared to the Y0.04 sample. The Y0.04 sample, due to the optimized amount of dopant, neither suffers from limited lattice space for lithium passage nor excessive distortions caused by guest atoms in the lattice. Consequently, it demonstrates consistent discharge capacity from the outset without significant fluctuations and achieves the highest discharge capacity among all samples. Overall, the Y0.04 sample exhibits the best charge/discharge performance over 100 cycles.

Table 6 highlights the differences in discharge capacity for the mentioned samples. As observed, adding carbon to the raw material results in a sudden increase in discharge capacity and a reduction in capacity fade. With the addition of non-optimized dopant elements, the discharge capacity further improves, but the capacity fade becomes worse compared to the LFP/C sample. Careful analysis of Table 6 reveals that by incorporating the optimal amount of dopants in the Y0.04 sample, the discharge capacity reaches its highest value in both the first and final cycles. Additionally, the capacity fade is reduced to 3.1 %, demonstrating significant improvement in cycling performance.

3.10. Rate capability analysis

Fig. 12(d) illustrates the rate capability of the optimized sample

Table 5
Comparison of the specific discharge capacity of the best composition found in this study with that obtained in the literature for the case of LFP coated with C.

Cathode composition	Specific Discharge Capacity	Synthesize Method	Ref.
$LiFe_{0.91}Y_{0.03}Nd_{0.06}PO_4/C$	150.1	solid-state	-
$Li_{0.99}Y_{0.01}FePO_4$	130	solid-state	[82]
$LiLa_{0.01}Fe_{0.99}PO_4/C$	156	solid-state	[83]
$LiCe_{0.1}Fe_{0.9}PO_4/C$	137	solid-state	[74]
$LiNd_{0.01}Fe_{0.99}PO_4/C$	115	solid-state	[84]
$LiSm_{0.06}Fe_{0.94}PO_4/C$	113	sol-gel	[85]
$LiEu_{0.02}Fe_{0.98}PO_4/C$	149	glass-ceramics quenching	[86]
$LiDy_{0.02}Fe_{0.98}PO_4/C$	110	sol-gel	[87]
$LiHo_{0.01}Fe_{0.99}PO_4/C$	160	solid-state	[88]
$LiEr_{0.02}Fe_{0.98}PO_4/C$	105	sol-gel	[89]
$LiYb_{0.02}Fe_{0.98}PO_4/C$	146	sol-gel	[90]
$LiW_{0.02}Fe_{0.98}PO_4/C$	110	solid-state	[91]
$LiPd_{0.02}Fe_{0.98}PO_4/C$	109	sol-gel	[92]
$LiFe_{0.975}Rh_{0.025}PO_4/C$	117	carbo thermal reduction	[93]
$LiRu_{0.01}Fe_{0.99}PO_4/C$	117	surfactant-assisted sol-gel	[94]
$LiMo_{0.01}Fe_{0.99}PO_4/C$	83	solid-state	[95]
$LiNb_{0.05}Fe_{0.95}PO_4/C$	85	sol-gel	[96]
$LiZn_{0.01}Fe_{0.99}PO_4/C$	133	solid-state	[97]
$LiCu_{0.02}Fe_{0.98}PO_4/C$	127	solid-state	[98]
$LiNi_{0.03}Fe_{0.97}PO_4/C$	94	spray drying and carbothermal reduction	[99]
$LiCo_{0.01}Fe_{0.99}PO_4/C$	115	sol-gel	[100]
$LiMn_{0.21}Fe_{0.79}PO_4/C$	108	reflux process and carbonization	[101]
$LiCr_{0.03}Fe_{0.97}PO_4/C$	120	mechanochemical	[102]
$LiV_{0.03}Fe_{0.97}PO_4/C$	117	sol-gel	[103]
$LiTi_{0.08}Fe_{0.92}PO_4/C$	110	solid-state	[104]
$LiSn_{0.03}Fe_{0.97}PO_4/C$	146	sol-gel	[105]
$LiIn_{0.01}Fe_{0.99}PO_4/C$	128	sol-gel	[106]
$Li_{0.99}Al_{0.01}FePO_4$	95	ceramic	[107]
$LiCa_{0.01}Fe_{0.99}PO_4/C$	80	solid-state	[108]
$Li_{0.95}Mg_{0.05}FePO_4$	108	solid-state	[109]
$Li_{0.97}K_{0.03}FePO_4$	76	carbothermal reduction	[110]
$LiNa_{0.01}Fe_{0.99}PO_4/C$	119	precipitation and spray drying	[111]

Table 6
Comparison of discharge capacities of different samples in their 1st and 100th cycle and their corresponding capacity fade.

Cathode Composition	Discharge Capacity (mAh/g)		Capacity Fade (%)
	Cycle 1	Cycle 100	
Bare LFP (Powder)	115	55	52
Bare LFP (Tablet)	124	80	35
LFP/C	135	100	26
$LiFe_{0.91}Y_{0.03}Nd_{0.06}PO_4/C$	152	137	10
$LiFe_{0.9}Y_{0.04}Nd_{0.06}PO_4/C$	159	149	6
$LiFe_{0.87}Y_{0.07}Nd_{0.06}PO_4/C$	146	128	12

Table 4
Comparison of the specific discharge capacity of different samples.

Cathode Composition	Bare LFP (Powder)	Bare LFP (Tablet)	LFP/C	$LiFe_{0.91}Y_{0.03}Nd_{0.06}PO_4/C$	$LiFe_{0.9}Y_{0.04}Nd_{0.06}PO_4/C$	$LiFe_{0.87}Y_{0.07}Nd_{0.06}PO_4/C$
Specific Discharge Capacity (mAh/g)	105.2	120.7	127.5	150.1	155.7	149.6

containing 0.04 yttrium and 0.06 neodymium. The sample underwent charging and discharging cycles at various rates of 0.1 C, 0.2 C, 0.5 C, 1 C, 2 C, and 5 C. It is observed that as the charging and discharging rate increases, the capacity decreases. At a 5 C rate, representing the highest charge rate, the discharge capacity reaches its minimum compared to other charging and discharging rates. This reduction indicates decreased electrical conductivity and increased electrode polarization at high rates (5 C) [112,113].

3.11. Electrochemical impedance analysis of LFP samples

The electrochemical impedance spectroscopy (EIS) analysis of the synthesized samples in this study was conducted using electrochemical cells under kinetic-diffusion control. All cells had identical anodes and electrolytes but different cathodes. This means that the solution resistance (R_s) was similar across all studies, while the charge-transfer resistance (R_{ct}), double-layer capacitance, and Warburg impedance varied. While EIS provides invaluable data regarding simple electrochemical systems, in the case of batteries, the results of this test are not interpretable that simply [114]. This is mainly due to the fact that various phenomena play a role during the working of a battery, including electron motions in electrodes, ion transport across a permeable passivation layer, charge transfer phenomena, diffusion in the solid state, and accumulation of charge on the electrode surface. Each of these phenomena occurs at a specific time scale and has an individual effect yet overlapping with that of others [115].

Fig. 13(a) illustrates the impedance diagrams of different samples, featuring a semicircular shape in the high-frequency area and a line that runs, ideally, at a 45° angle in the lower frequency area. However, in most of the experiments, this line will have a slope somewhere between 35° and 55° [116]. The observed semicircle arises from the combination of two semicircles: one situated in the high-frequency domain and the other in the mid-frequency domain. The high-frequency region's semicircular shape indicates the flux of lithium ions across the interfacial layer at the electrode/electrolyte interface, which corresponds to R_f in the equivalent circuit. The semicircle observed in the mid-frequency region corresponds to the charge transfer resistance (R_{ct}), indicating the intricate dynamics of charge transfer reactions occurring between the electrolyte and active materials. The low-frequency region's linear behavior, which corresponds to (W) in the equivalent circuit, indicates the diffusion process of lithium ions throughout the bulk of the electrode material. In conclusion, the diameter of the semicircle corresponds to the sum of R_f and R_{ct}, while the slope of the straight line reflects the extent of lithium-ion diffusion within the LFP structure. Furthermore, the constant phase elements (CPE) relate to the pseudo-capacitive characteristics of the oxide layer that develops between the electrode and electrolyte, and they are taken into account in parallel with R_f and R_{ct} within the equivalent circuit [117].

With closer examination of Fig. 13(a), it can be observed that adding carbon and dopant elements to the material reduces the diameter of the semicircle from approximately 14 mΩ in the raw sample to about 2 mΩ in the $LFPY_{0.04}$ $Nd_{0.06}$/C sample. This reduction indicates a decrease in R_f and R_{ct}, attributed to improved lithium-ion diffusion at the electrode/electrolyte interface and enhanced electrical conductivity due to the addition of carbon. Thus, it can be concluded that by optimally applying a carbon layer and adding dopants, the cathode impedance is reduced, leading to enhanced charge/discharge capacity. Based on Eq. (10) [73], a measure of $R_{ct} + R_f$ and D_{Li} was calculated and reported in Table 7. As can be seen, the doping of LFP/C up to the optimum value resulted in a continuous decrease in the charge transfer resistance as well as a consistent increase in the diffusivity of Li.

$$D = \frac{R^2T^2}{2A^2n^4F^2c^2\sigma_w^2} \tag{10}$$

In this equation,

- D represents the diffusivity of Li
- n represents the number of electrons
- T represents the absolute temperature (K)
- A represents the surface area of the working electrode
- F is the Faraday constant
- c represents the concentration of Li
- σ_w represents the Warburg factor

Fig. 13(b), on the other hand, depicts the electrochemical impedance spectra of samples after they went through 100 cycles. As can be seen, cycling resulted in the shift of the curves along the Z' axis, which means an increase in the ohmic resistance (Rs). Several components play a role in determining this resistance, including electrolyte, electrode particles, and current collectors. In this manner, upon the operation of the cell, factors such as electrolyte decomposition, corrosion of the current

Table 7
Comparison of the effect of doping on the charge transfer resistance and D_{Li}.

Cathode Composition	Solution Resistance (mΩ)	Charge Resistance (mΩ)	D_{Li} (cm^2/s)
LFP/C	0.33	6.7	1.73×10^{-14}
$LiFe_{0.91}Y_{0.03}Nd_{0.06}PO_4$/C	0.32	2.3	4.56×10^{-14}
$LiFe_{0.9}Y_{0.04}Nd_{0.06}PO_4$/C	0.29	1.7	9.83×10^{-14}
$LiFe_{0.87}Y_{0.07}Nd_{0.06}PO_4$/C	0.37	5.6	1.58×10^{-14}

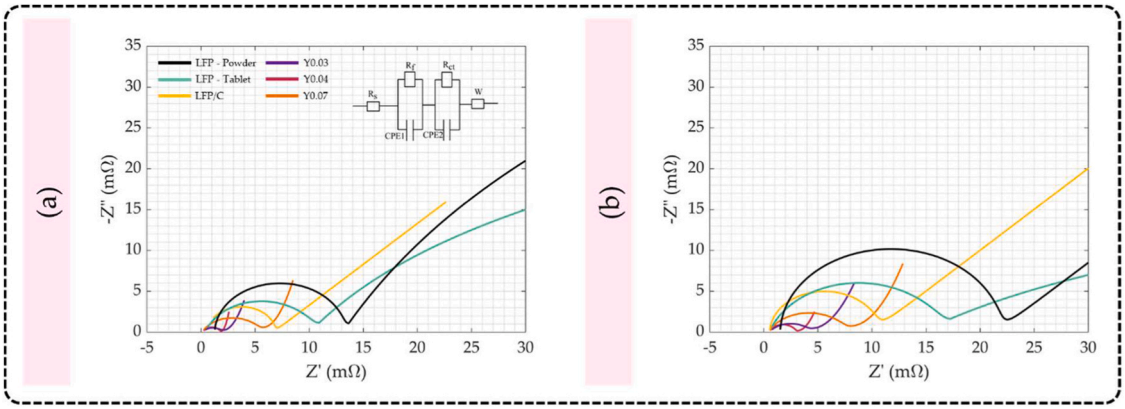

Fig. 13. Nyquist diagrams of cells with different synthesized cathode materials and the effect of doping (a) before cycling and (b) after cycling (the inset depicts the equivalent circuit).

collectors, SEI growth, and Li plating on the negative electrode can increase Rs. Moreover, it is observable that the radius of the semiarch at the mid- to low-frequency regions also increased for all samples. This region corresponds to the charge-transfer process, and its enlargement after cycling can be attributed to CEI formation and retardation of charge transfer as well as SEI growth and decomposition. However, as it is evident from these figures, even after 100 cycles, doped structures outperformed pristine LFP and LFP/C specimens. This is in complete accordance with the results given in Fig. 12(c), where it was observed that the doped specimens show high levels of cyclic stability.

3.12. Analysis of synergy

Having established the properties of the synthesized unique LFP/C specimens co-doped with Nd and Y, it is now pertinent to consolidate the data and conduct the study that was intended. Fig. 14(a) illustrates the SDC of various co-doped LFP/C specimens sourced from literature [55–57,118,119], juxtaposed with their corresponding anticipated SDC derived from the established GPR—Scheme 2, by aggregating the individual contributions of their dopants. All data points are positioned above the bisector of the first quadrant, indicating a synergistic impact between the two co-dopants. These data, although limited, were used to train a GPR model to predict the effect of the reduced input features for both co-dopants (i.e., $Z_{heavier\ dopant}$, $V_{heavier\ dopant}$, ..., $\chi_{heavier\ dopant}$, $Z_{lighter\ dopant}$, $V_{lighter\ dopant}$, ..., $\chi_{lighter\ dopant}$) on the difference between actual SDC values and those obtained from summing the individual effects of each dopant, obtained from previously trained GPR model (i.e., GPR – Scheme 2). This GPR model was called GPR – Scheme 3, and Fig. 14(b) illustrates the efficiency of this trained model ($R^2 = 0.904$). Through simultaneous application of GPR – Scheme 2 and GPR – Scheme 3, the SDCs of the synthesized active materials in this study were calculated. Fig. 14(c) compares the actual and anticipated values, and it can be seen that while the adopted ML strategy does not preserve the order of materials in term of their corresponding SDC, predicted values are in good accordance with the actual values.

4. Conclusion

This study successfully demonstrated the application of machine learning techniques to evaluate and predict the synergistic effects of co-doped elements in $LiFePO_4$/C cathode materials for LiBs. The main outcomes of this study can be summarized as:

- The Pearson correlation coefficient matrix analysis indicated that the difference between a dopant's atomic radius and the atomic radius of either Li or Fe could be a good measure to predict the effect of that element on the SDC of LFP/C.
- It was shown that the difference between an element's radius with the radius of Fe is as effective as its difference with that of Li. In this regard, no prominent role can be imagined for either Li or Fe.
- Between RF and GPR, it was demonstrated that the GPR model is more efficient in predicting the effect of a doped element on the SDC of LFP.
- Due to the lack of data in the existing literature regarding low-efficient doped structures, it was shown that it would be challenging to train a model capable of attaining the most comprehensive view of the effect of a wide range of elements on the SDC of LFP.
- It was shown that the addition of Yttrium up to 0.04 in the presence of 0.06 Nd can significantly enhance the electrochemical performance of LFP/C.

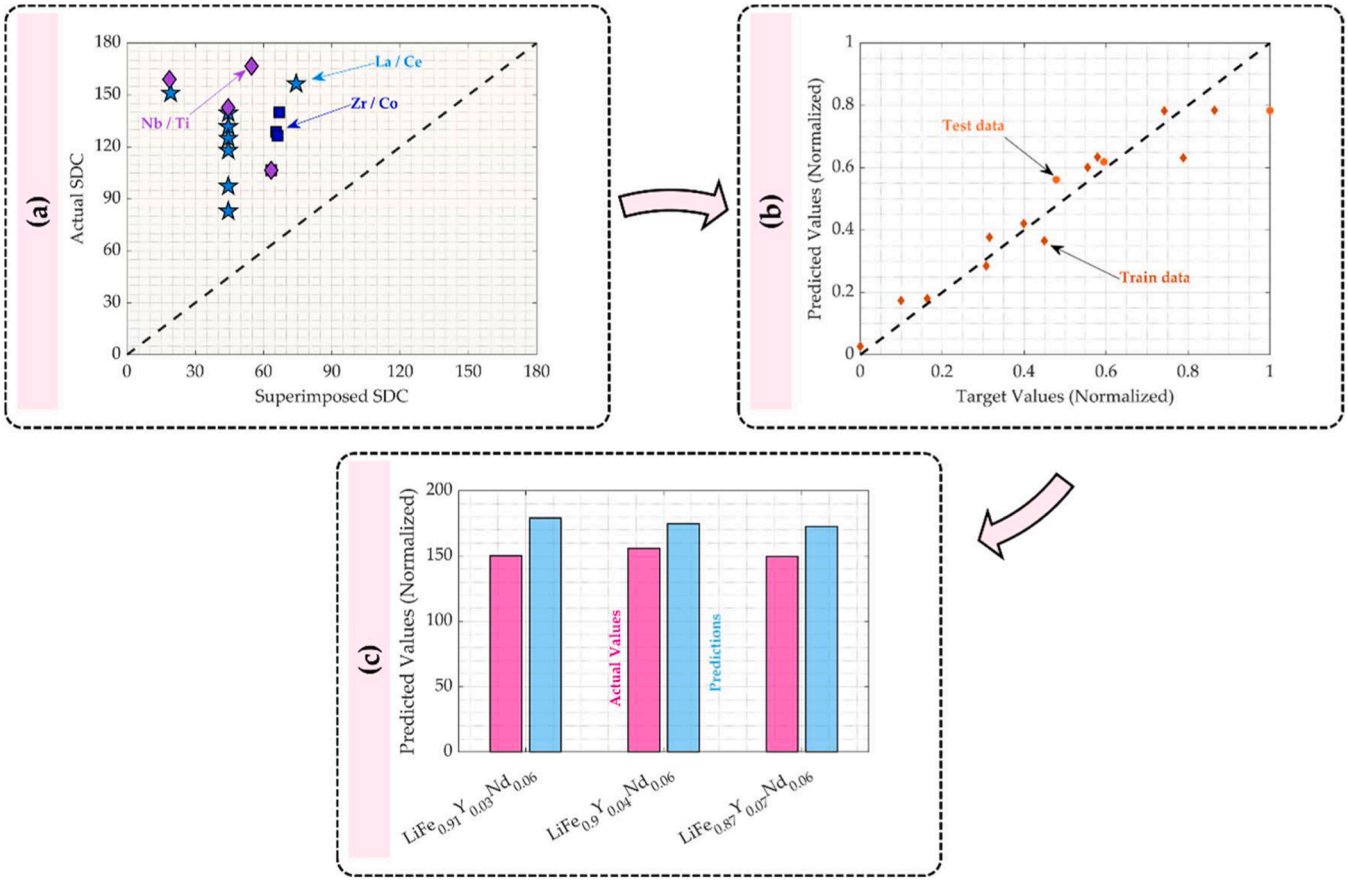

Fig. 14. (a) comparison of the actual and predicted normalized SDC of various co-doped LFP/C materials, (b) the results of the trained ML scheme, and (c) a comparison of the developed ML scheme for studying synergy with the obtained experimental results.

- It was demonstrated that co-doping is nearly almost associated with a synergic effect. In this essence, the addition of two co-dopants will be more successful in enhancing the electrochemical performance of LFP/C compared to the individual effect of each dopant that it may have.
- Inspired by the ML models developed to correlate the physi-ochemical properties of single elements on the SDC of LFP/C, another ML model was developed to find the effect of the respective properties of co-dopants on the deviation of the SDC of resulting composition from predictions.
- A comparison of the results obtained from the ML model trained to capture synergy with the experimentally found values demonstrated acceptable performance of the developed ML scheme.

CRediT authorship contribution statement

Ali A. Javidparvar: Writing – review & editing, Writing – original draft, Validation, Software, Investigation, Data curation. **Mohammed M. Alammar:** Software, Methodology, Investigation, Formal analysis. **Amuthakkannan Rajakannu:** Software, Resources, Investigation, Conceptualization. **Z.M.S. Elbarbary:** Writing – review & editing, Writing – original draft, Methodology, Investigation, Conceptualization. **Priya A. Hoskeri:** Validation, Software, Resources, Investigation, Data curation. **Theodore Azemtsop Manfo:** Writing – review & editing, Writing – original draft, Supervision, Methodology, Investigation, Conceptualization, Project administration, Validation, Visualization.

Declaration of Competing Interest

The authors declare that they have no known competing financial interests or personal relationships that could have appeared to influence the work reported in this paper.

Acknowledgements

The authors extend their appreciation to the Deanship of Scientific Research at King Khalid University for funding this work through the General Research Project under Grant number (RGP2/388/46).

References

[1] C.Y. Hsu, Y. Ajaj, G.K. Ghadir, H.M. Al-Tmimi, Z.K. Alani, A.A. Almulla, M. A. Hussein, A.R. Al-Tameemi, Z.H. Mahmoud, M. Ahmed mustafa, F. Kianfar, S. Habibzadeh, E. Kianfar, Rechargeable batteries for energy storage: a review, E-Prime - Adv. Electr. Eng. Electron. Energy 8 (2024) 100510, https://doi.org/10.1016/j.prime.2024.100510.

[2] B. Mosallanejad, M. Akrami, Recent advances on electrolyte additives used in lead-acid batteries to enhance their electrochemical performances, J. Energy Storage 97 (2024) 112738, https://doi.org/10.1016/j.est.2024.112738.

[3] Q. Abbas, M. Mirzaeian, M.R.C. Hunt, P. Hall, R. Raza, Current state and future prospects for electrochemical energy storage and conversion systems, Energies 13 (2020) 5847, https://doi.org/10.3390/en13215847.

[4] M. Ikoma, A. Ohta, Current status and future prospect for Ni/MH battery, Electrochemistry 68 (2000) 1010–1011.

[5] H. Rostami, J. Valio, P. Suominen, P. Tynjälä, U. Lassi, Advancements in cathode technology, recycling strategies, and market dynamics: a comprehensive review of sodium ion batteries, Chem. Eng. J. 495 (2024) 153471, https://doi.org/10.1016/j.cej.2024.153471.

[6] K. Kumar, R. Kundu, Empowering energy storage technology: recent breakthroughs and advancement in sodium-ion batteries, ACS Appl. Energy Mater. 7 (2024) 3523–3539, https://doi.org/10.1021/acsaem.4c00592.

[7] T. Sharmin, N. Hossain, F.T. Mohsin, M.A. Haque, M.M. Mashfy, T.A. Alvy, M. Nasim, Advancements in cutting-edge materials for sodium-ion battery anodes: a comprehensive review, Mater. Today Chem. 42 (2024) 102407, https://doi.org/10.1016/j.mtchem.2024.102407.

[8] O. Dolotko, N. Gehrke, M. Knapp, H. Ehrenberg, Mechanochemically induced hydrometallurgical method for recycling d-elements from Li-ion battery cathodes, J. Alloy. Compd. 976 (2024) 172884, https://doi.org/10.1016/j.jallcom.2023.172884.

[9] M. Torabi, S.K. Sadrnezhaad, Nanostructured-microfibrillar polypyrrole coated NiTi current collectors for high power and shape memory LiFePO4 cathodes for Li-ion batteries, J. Alloy. Compd. 969 (2023) 172467, https://doi.org/10.1016/j.jallcom.2023.172467.

[10] M. Zhao, Y. Wang, Y. Wang, S. Liu, Z. Chen, F. Yong, P. Qian, S. Yang, Q. Huang, Z. Ning, PO43–doped layer @ spinel @ rGO sandwich-structured lithium-rich manganese-based cathode material with enhancing rate capability and cycle stability for Li-ion battery, J. Alloy. Compd. 983 (2024) 173822, https://doi.org/10.1016/j.jallcom.2024.173822.

[11] W. Wang, C. Lin, F. Luo, R. Liu, X. Chen, W. Wu, S. Wei, F. Xiao, P. Xiong, Q. Chen, Q. Qian, L. Zeng, VO2/MoS2 heterostructure synergized oxygen vacancies as a cathode material for high-performance hybrid Mg/Li-ion batteries over a wide temperature range, J. Alloy. Compd. 1010 (2025) 178281, https://doi.org/10.1016/j.jallcom.2024.178281.

[12] G. Zubi, R. Dufo-López, M. Carvalho, G. Pasaoglu, The lithium-ion battery: State of the art and future perspectives, Renew. Sustain. Energy Rev. 89 (2018) 292–308, https://doi.org/10.1016/j.rser.2018.03.002.

[13] J.B. Goodenough, K.S. Park, The Li-ion rechargeable battery: a perspective, J. Am. Chem. Soc. 135 (2013) 1167–1176, https://doi.org/10.1021/ja3091438.

[14] Z. Yang, J. Zhang, M.C.W. Kintner-Meyer, X. Lu, D. Choi, J.P. Lemmon, J. Liu, Electrochemical energy storage for green grid, Chem. Rev. 111 (2011) 3577–3613, https://doi.org/10.1021/cr100290v.

[15] A. Huang, M.F. El-Kady, X. Chang, M. Anderson, C.W. Lin, C.L. Turner, R. B. Kaner, Facile fabrication of multivalent VOx/graphene nanocomposite electrodes for high-energy-density symmetric supercapacitors, Adv. Energy Mater. 11 (2021), https://doi.org/10.1002/aenm.202100768.

[16] Y. Mao, W. Sun, X. Yue, W. Hou, T. Deng, L. He, L. Fang, R. Sun, Z. Wang, K. Sun, Flexible free-standing cathode enabled via multifunctional Mo2C for high sulfur loading lithium–sulfur batteries, J. Power Sources 506 (2021) 230254, https://doi.org/10.1016/j.jpowsour.2021.230254.

[17] Y. Li, P.C. Zhao, B. Shen, A review of new technologies for lithium-ion battery treatment, Sci. Total Environ. 951 (2024) 175459, https://doi.org/10.1016/j.scitotenv.2024.175459.

[18] W. Chen, Y. Zhao, J. Zhou, S. Li, C. Lu, S. Zhou, H. Li, Y. Li, Y. Cheng, J. Yang, Y. He, J. Luo, High-throughput screening of halide solid-state electrolytes for all-solid-state Li-ion batteries through structural descriptor, J. Alloy. Compd. 1010 (2025) 177167, https://doi.org/10.1016/j.jallcom.2024.177167.

[19] A. Dixit, Cathode materials for lithium ion batteries (LIBs): a review on materials related aspects towards, High. Energy Density LIBs (2020).

[20] J.-J. Marie, Developments in lithium-ion battery cathodes, Faraday Insights-Issue 18 (2023) 1–12.

[21] A.K. Koech, G. Mwandila, F. Mulolani, P. Mwaanga, Lithium-ion battery fundamentals and exploration of cathode materials: a review, South Afr. J. Chem. Eng. 50 (2024) 321–339, https://doi.org/10.1016/j.sajce.2024.09.008.

[22] W. Fu, Y. Wang, K. Kong, D. Kim, F. Wang, G. Yushin, Materials and processing of lithium-ion battery cathodes, Nanoenergy Adv. 3 (2023) 138–154, https://doi.org/10.3390/nanoenergyadv3020008.

[23] S. Ghosh, U.B. charjee, S. Bhowmik, S.K. Martha, A review on high-capacity and high-voltage cathodes for next-generation lithium-ion batteries, J. Energy Power Technol. 4 (2021) 1-1, https://doi.org/10.21926/jept.2201002.

[24] H. Shou, X. Cui, Cycle life and influencing factors of cathode materials for lithium-ion batteries - A case study of lithium-cobalt oxides, Appl. Math. Nonlinear Sci. 9 (2024), https://doi.org/10.2478/amns-2024-1285.

[25] A. Kitajou, S. Matsuda, K. Ohara, K. Ikeda, S. Muto, Cathode properties of a controlled crystallinity nano-Li 1.2 Cr 0.4 Mn 0.4 O 2 cathode for lithium ion batteries, RSC Mechanochemistry (2025), https://doi.org/10.1039/D4MR00051J.

[26] J. Hu, H. Wang, B. Xiao, P. Liu, T. Huang, Y. Li, X. Ren, Q. Zhang, J. Liu, X. Ouyang, X. Sun, Challenges and approaches of single-crystal Ni-rich layered cathodes in lithium batteries, Natl. Sci. Rev. 10 (2023), https://doi.org/10.1093/nsr/nwad252.

[27] M. Li, J. Lu, Z. Chen, K. Amine, 30 years of lithium-ion batteries, Adv. Mater. 30 (2018), https://doi.org/10.1002/adma.201800561.

[28] J. Hu, W. Huang, L. Yang, F. Pan, Structure and performance of the LiFePO4cathode material: From the bulk to the surface, Nanoscale 12 (2020) 15036–15044, https://doi.org/10.1039/d0nr03776a.

[29] L.X. Yuan, Z.H. Wang, W.X. Zhang, X.L. Hu, J.T. Chen, Y.H. Huang, J. B. Goodenough, Development and challenges of LiFePO4 cathode material for lithium-ion batteries, Energy Environ. Sci. 4 (2011) 269–284, https://doi.org/10.1039/c0ee00029a.

[30] L. Minnetti, V. Marangon, J. Hassoun, Synthesis and Characterization of a LiFe0.6Mn0.4PO4 Olivine Cathode for Application in a New Lithium Polymer Battery, Adv. Sustain. Syst. 6 (2022), https://doi.org/10.1002/adsu.202100464.

[31] W.J. Zhang, Structure and performance of LiFePO4 cathode materials: a review, J. Power Sources 196 (2011) 2962–2970, https://doi.org/10.1016/j.jpowsour.2010.11.113.

[32] D. Hou, J. Chen, F. Bai, F. Meng, P. Dong, C. Zhang, Y. Zhang, J. Hu, Efficient regeneration of waste LiFePO4 cathode material by short process low temperature plasma assisted nitrogen doped technology, J. Power Sources 613 (2024) 234845, https://doi.org/10.1016/j.jpowsour.2024.234845.

[33] Z. Ahsan, B. Ding, Z. Cai, C. Wen, W. Yang, Y. Ma, S. Zhang, Recent progress in capacity enhancement of LiFePO4cathode for Li-Ion batteries, J. Electrochem. Energy Convers. Storage 18 (2021), https://doi.org/10.1115/1.4047222.

[34] H. Seo, J. Kang, H. Kim, S. Jang, J.H. Kim, S. Choi, H. Eom, O. Kwon, J. Shin, J. Park, D. Yoo, S. Jeong, S.H. Noh, C.W. Park, M.L. Seol, S. Park, I. Nam, Enhancing the performance of LiFePO4 cathodes in Li-ion batteries: role of surface coating based on ZIF-8 particle size optimization, Korean J. Chem. Eng. (2024), https://doi.org/10.1007/s11814-024-00215-0.

[35] L. Wang, H. Chen, Y. Zhang, J. Liu, L. Peng, Research Progress in Strategies for Enhancing the Conductivity and Conductive Mechanism of LiFePO4 Cathode

Materials, Molecules 29 (2024) 5250, https://doi.org/10.3390/molecules29225250.
[36] L. Yang, Y. Tian, J. Chen, J. Gao, Z. Long, W. Deng, G. Zou, H. Hou, X. Ji, A high-rate capability LiFePO4/C cathode achieved by the modulation of the band structures, J. Mater. Chem. A. 9 (2021) 24686–24694, https://doi.org/10.1039/d1ta07757k.
[37] C. Cheng, Enhancing the Sustainability of LiFePO4/C with High Performance Via Employing Lignin as Reduction Agent, Metall. Mater. Trans. B Process. Metall. Mater. Process. Sci. (2024), https://doi.org/10.1007/s11663-024-03389-4.
[38] Y. Li, J. Wang, C.C. Fu, X. Li, L.L. Wang, LiFePO4/C nanoparticle with fast ion/electron transfer capability obtained by adjusting pH values, J. Mater. Sci. 56 (2021) 640–648, https://doi.org/10.1007/s10853-020-05192-3.
[39] W. Lin, P. Yang, K. Zhou, L. Wang, C. Shen, Indium doping: An effective route to optimize the electrochemical performance of LiFePO4 cathode material, Solid State Ion. 403 (2023) 116322, https://doi.org/10.1016/j.ssi.2023.116322.
[40] S.Y. Chung, J.T. Bloking, Y.M. Chiang, Electronically conductive phospho-olivines as lithium storage electrodes, Nat. Mater. 1 (2002) 123–128, https://doi.org/10.1038/nmat732.
[41] E. Strauss, S. Menkin, D. Golodnitsky, On the way to high-conductivity single lithium-ion conductors, J. Solid State Electrochem 21 (2017) 1879–1905, https://doi.org/10.1007/s10008-017-3638-8.
[42] M.M. Raju, F. Altayran, M. Johnson, D. Wang, Q. Zhang, Crystal structure and preparation of Li7La3Zr2O12 (LLZO) solid-state electrolyte and doping impacts on the conductivity: an overview, Electrochem 2 (2021) 390–414, https://doi.org/10.3390/electrochem2030026.
[43] Y. Zhang, J.A. Alarco, J.Y. Nerkar, A.S. Best, G.A. Snook, P.C. Talbot, Improving the rate capability of LiFePO 4 electrode by controlling particle size distribution, J. Electrochem. Soc. 166 (2019) A4128–A4135, https://doi.org/10.1149/2.0621916jes.
[44] J. Hong, W. Wei, G. He, Optimizing the particle-size distribution and tap density of LiFePO4/C composites containing excess lithium, Ion. (Kiel.) 25 (2019) 2035–2039, https://doi.org/10.1007/s11581-018-2683-3.
[45] H. Zhang, Z. Zou, S. Zhang, J. Liu, S. Zhong, A review of the doping modification of LiFePO4 as a cathode material for lithium ion batteries, Int. J. Electrochem. Sci. 15 (2020) 12041–12067, https://doi.org/10.20964/2020.12.71.
[46] N. Kuganathan, A. Chroneos, Formation, doping, and lithium incorporation in LiFePO4, AIP Adv. 12 (2022), https://doi.org/10.1063/5.0087765.
[47] X. Jiang, Y. Xin, B. He, F. Zhang, H. Tian, Effect of heteroatom doping on electrochemical properties of olivine LiFePO4 cathodes for high-performance lithium-ion batteries, Mater. (Basel) 17 (2024) 1299, https://doi.org/10.3390/ma17061299.
[48] Caleb Omata Ilabija, Temitope Olubanjo Kehinde, Jude Ifeanyichukwu Ishiwu, Oluwafemi Tayo Ojo, Shola Abayomi Ogunkanmi, Muhammad Bolakale Salman, Afolabi Ridwan Bello, Advances in nanomaterials for lithium-ion batteries: enhancing energy density and lifespan, World J. Adv. Eng. Technol. Sci. 13 (2024) 560–588, https://doi.org/10.30574/wjaets.2024.13.2.0631.
[49] Y. Huang, Y. Xu, X. Yang, Enhanced electrochemical performances of LiFePO4/C by co-doping with magnesium and fluorine, Electrochim. Acta 113 (2013) 156–163, https://doi.org/10.1016/j.electacta.2013.09.044.
[50] H. Liu, M.J. Choe, R.A. Enrique, B. Orvañanos, L. Zhou, T. Liu, K. Thornton, C. P. Grey, Effects of antisite defects on Li diffusion in LiFePO4 revealed by Li isotope exchange, J. Phys. Chem. C. 121 (2017) 12025–12036, https://doi.org/10.1021/acs.jpcc.7b02819.
[51] J. Hu, J. Xie, X. Zhao, H. Yu, X. Zhou, G. Cao, J. Tu, Doping effects on electronic conductivity and electrochemical performance of LiFePO4, J. Mater. Sci. Technol. 25 (2009) 405–409.
[52] C. Yao, F. Wang, J. Chen, M. Yin, First-principles study of the structural and electronic properties of LiFePO4 by graphene and N-doped graphene modification, Comput. Theor. Chem. 1217 (2022) 113897, https://doi.org/10.1016/j.comptc.2022.113897.
[53] Y. Li, L. Wang, F. Liang, Y. Yao, K. Zhang, Enhancing high rate performance and cyclability of LiFePO4 cathode materials for lithium ion batteries by boron doping, J. Alloy. Compd. 880 (2021) 160560, https://doi.org/10.1016/j.jallcom.2021.160560.
[54] S. Kandhasamy, K. Nallathamby, M. Minakshi, Role of structural defects in olivine cathodes, Prog. Solid State Chem. 40 (2012) 1–5, https://doi.org/10.1016/j.progsolidstchem.2012.01.001.
[55] B. Zhang, X. Ma, W. Hou, W. Yuan, L. He, O. Yang, Y. Liu, J. Wang, Y. Xu, Revealing the Ultrahigh Rate Performance of the La and Ce Co-doping LiFePO4Composite, ACS Appl. Energy Mater. 5 (2022) 14712–14719, https://doi.org/10.1021/acsaem.2c02035.
[56] Z. Tian, Z. Zhou, S. Liu, F. Ye, S. Yao, Enhanced properties of olivine LiFePO4/graphene co-doped with Nb5 + and Ti4 + by a sol-gel method, Solid State Ion. 278 (2015) 186–191, https://doi.org/10.1016/j.ssi.2015.06.017.
[57] L. Gao, Z. Xu, S. Zhang, The co-doping effects of Zr and Co on structure and electrochemical properties of LiFePO4 cathode materials, J. Alloy. Compd. 739 (2018) 529–535, https://doi.org/10.1016/j.jallcom.2017.12.313.
[58] Z.H. Wang, L.X. Yuan, M. Wu, D. Sun, Y.H. Huang, Effects of Na+ and Cl- co-doping on electrochemical performance in LiFePO4/C, Electrochim. Acta 56 (2011) 8477–8483, https://doi.org/10.1016/j.electacta.2011.07.018.
[59] X. Li, L. Yu, Y. Cui, A. Li, H. Shao, Z. Shao, W. Zhang, Z. Shao, Enhanced properties of LiFePO4/C cathode materials co-doped with V and F ions via high-temperature ball milling route, Int. J. Hydrog. Energy 44 (2019) 27204–27213, https://doi.org/10.1016/j.ijhydene.2019.08.187.
[60] S.H. Kwak, Y.J. Park, Improving the Performance of LiFePO4 Cathodes with a Sulfur-Modified Carbon Layer, Batteries 10 (2024) 348, https://doi.org/10.3390/batteries10100348.
[61] P.M. Pratheeksha, E.H. Mohan, B.V. Sarada, M. Ramakrishna, K. Hembram, P.V. V. Srinivas, P.J. Daniel, T.N. Rao, S. Anandan, Development of a novel carbon-coating strategy for producing core-shell structured carbon coated LiFePO4 for an improved Li-ion battery performance, Phys. Chem. Chem. Phys. 19 (2017) 175–188, https://doi.org/10.1039/c6cp06923a.
[62] Z. Chen, Q. Zhang, Q. Liang, Carbon-coatings improve performance of Li-ion battery, Nanomaterials 12 (2022) 1936, https://doi.org/10.3390/nano12111936.
[63] X. Zhi, G. Liang, X. Ou, S. Zhang, L. Wang, Synthesis and Electrochemical Performance of LiFePO 4 /C Composite by Improved Solid-State Method Using a Complex Carbon Source, J. Electrochem. Soc. 164 (2017) A1285–A1290, https://doi.org/10.1149/2.1511706jes.
[64] M. Kroff, S.A. Hevia, J.N. O'Shea, I.G. de Muro, V. Palomares, T. Rojo, R. del Río, Lithium iron phosphate/carbon (LFP/C) composite using nanocellulose as a reducing agent and carbon source, Polym. (Basel) 15 (2023) 2628, https://doi.org/10.3390/polym15122628.
[65] N. Gupta, R. Kumar, A. Alankar, Machine learning–based discovery of novel oxide and halide perovskites for energy storage, J. Alloy. Compd. 1010 (2025) 177470, https://doi.org/10.1016/j.jallcom.2024.177470.
[66] T.L. Achmad, P.A. Wibowo, F.T. Sukma, Design of high entropy superalloy FeNiCrCoAl using molecular dynamics, computational thermodynamics, and machine learning, J. Alloy. Compd. 1010 (2025) 177514, https://doi.org/10.1016/j.jallcom.2024.177514.
[67] Y. Sun, B. Hu, Y. Zhang, X. Song, J. Feng, Y. Xu, H. Tao, D. Ergu, Machine learning-assisted accelerated research on piezoelectric response prediction of KNN-based ceramics, J. Alloy. Compd. 1003 (2024) 175598, https://doi.org/10.1016/j.jallcom.2024.175598.
[68] G. Wang, T. Fearn, T. Wang, K.L. Choy, Machine-learning approach for predicting the discharging capacities of doped lithium nickel-cobalt-manganese cathode materials in Li-ion batteries, ACS Cent. Sci. 7 (2021) 1551–1560, https://doi.org/10.1021/acscentsci.1c00611.
[69] C. Lv, X. Zhou, L. Zhong, C. Yan, M. Srinivasan, Z.W. Seh, C. Liu, H. Pan, S. Li, Y. Wen, Q. Yan, Machine learning: an advanced platform for materials development and state prediction in lithium-ion batteries, Adv. Mater. 34 (2022), https://doi.org/10.1002/adma.202101474.
[70] H. Alzamer, R. Jaafreh, J.G. Kim, K. Hamad, Artificial intelligence and Li ion batteries: basics and breakthroughs in electrolyte materials discovery, Crystals 15 (2025) 114, https://doi.org/10.3390/cryst15020114.
[71] P. Deeg, C. Weisenberger, J. Oehm, D. Schmidt, O. Csiszar, V. Knoblauch, Swift prediction of battery performance: applying machine learning models on microstructural electrode images for lithium-ion batteries, Batteries 10 (2024) 99, https://doi.org/10.3390/batteries10030099.
[72] A. Valizadeh, M.H. Amirhosseini, Machine learning in lithium-ion battery: applications, challenges, and future trends, SN Comput. Sci. 5 (2024) 717, https://doi.org/10.1007/s42979-024-03046-2.
[73] H. Yuan, X. Wang, Q. Wu, H. Shu, X. Yang, Effects of Ni and Mn doping on physicochemical and electrochemical performances of LiFePO4/C, J. Alloy. Compd. 675 (2016) 187–194, https://doi.org/10.1016/j.jallcom.2016.03.065.
[74] N. Zhao, Y. Li, X. Zhi, L. Wang, X. Zhao, Y. Wang, G. Liang, Effect of Ce3+ doping on the properties of LiFePO4 cathode material, J. Rare Earths 34 (2016) 174–180, https://doi.org/10.1016/S1002-0721(16)60011-X.
[75] F. Hasan, J. Kim, H. Song, S.H. Lee, J.H. Sung, J. Kim, H.D. Yoo, Effect of particle size and doping on the electrochemical characteristics of Ca-doped LiCoO2 cathodes, J. Electrochem. Sci. Technol. 11 (2020) 352–360, https://doi.org/10.33961/jecst.2020.00899.
[76] T. Sattar, S.H. Lee, B.S. Jin, H.S. Kim, Influence of Mo addition on the structural and electrochemical performance of Ni-rich cathode material for lithium-ion batteries, Sci. Rep. 10 (2020) 8562, https://doi.org/10.1038/s41598-020-64546-8.
[77] H.H. Ryu, S.B. Lee, Y.K. Sun, Promoting grain growth in Ni-rich single-crystal cathodes for high-performance lithium-ion batteries through Ce doping, J. Solid State Electrochem 26 (2022) 2097–2105, https://doi.org/10.1007/s10008-022-05212-z.
[78] C. Misiewicz, K. Edstrom, E.J. Berg, Formation of a cathode electrolyte interphase on high-voltage Li-ion cathodes, Chem. Mater. 36 (2024) 9729–9740, https://doi.org/10.1021/acs.chemmater.4c01872.
[79] K. Abe, Y. Ushigoe, H. Yoshitake, M. Yoshio, Functional electrolytes: Novel type additives for cathode materials, providing high cycleability performance, J. Power Sources 153 (2006) 328–335, https://doi.org/10.1016/j.jpowsour.2005.05.067.
[80] S.K.Vineeth Sungjemmenla, C.B. Soni, V. Kumar, Z.W. Seh, Understanding the cathode–electrolyte interphase in lithium-ion batteries, Energy Technol. 10 (2022), https://doi.org/10.1002/ente.202200421.
[81] S.P. Kühn, K. Edström, M. Winter, I. Cekic-Laskovic, Face to face at the cathode electrolyte interphase: from interface features to interphase formation and dynamics, Adv. Mater. Interfaces 9 (2022), https://doi.org/10.1002/admi.202102078.
[82] Y.Da Cho, G.T.K. Fey, H.M. Kao, Physical and electrochemical properties of La-doped LiFePO4/C composites as cathode materials for lithium-ion batteries, J. Solid State Electrochem 12 (2008) 815–823, https://doi.org/10.1007/s10008-007-0498-7.

[83] Y. TIAN, X. KANG, L. LIU, C. XU, T. QU, Research on cathode material of Li-ion battery by yttrium doping, J. Rare Earths 26 (2008) 279–283, https://doi.org/10.1016/S1002-0721(08)60081-2.
[84] Q. Zhang, S. Wang, Z. Zhou, G. Ma, W. Jiang, X. Guo, S. Zhao, Structural and electrochemical properties of Nd-doped LiFePO4/C prepared without using inert gas, Solid State Ion. 191 (2011) 40–44, https://doi.org/10.1016/j.ssi.2011.03.025.
[85] X. Meng, B. Han, Y. Wang, J. Nan, Effects of samarium doping on the electrochemical performance of LiFePO4/C cathode material for lithium-ion batteries, Ceram. Int. 42 (2016) 2599–2604, https://doi.org/10.1016/j.ceramint.2015.10.063.
[86] S. Altin, M. Coban, S. Altundag, E. Altin, Production of Eu-doped LiFePO4 by glass–ceramic technique and investigation of their thermal, structural, electrochemical performances, J. Mater. Sci. Mater. Electron 33 (2022) 13720–13730, https://doi.org/10.1007/s10854-022-08305-7.
[87] H. Göktepe, Effect of Dy3+ -doping on electrochemical properties of LiFePO4/C cathode for lithium-ion batteries, J. Chin. Chem. Soc. 60 (2013) 218–222, https://doi.org/10.1002/jccs.201200266.
[88] S. Altin, A. Yolun, Fabrication and electrochemical performance of Ho-substituted C/LiFePO4: improved battery performance, J. Mater. Sci. Mater. Electron 32 (2021) 21568–21578, https://doi.org/10.1007/s10854-021-06665-0.
[89] H. Göktepe, H. Sahan, A. Ülgen, Ş. Patat, Synthesis and electrochemical properties of carbon-mixed LiEr0.02Fe0.98PO4 cathode material for lithium-ion batteries, J. Mater. Sci. Technol. 27 (2011) 861–864, https://doi.org/10.1016/S1005-0302(11)60156-4.
[90] H. Göktepe, Electrochemical performance of Yb-doped LiFePO4/C composites as cathode materials for lithium-ion batteries, Res. Chem. Inter. 39 (2013) 2979–2987, https://doi.org/10.1007/s11164-012-0811-7.
[91] H. Arava, H. Fang, L.L. Zhang, J.W. Hill, G. Liang, Electrochemical studies of carbon coated LiFePO4 doped with tungsten. in: Proc. IEEE Conf. Nanotechnol, IEEE, 2013, pp. 1050–1053, https://doi.org/10.1109/NANO.2013.6720943.
[92] M. Talebi-Esfandarani, O. Savadogo, Effects of palladium doping on the structure and electrochemical properties of LiFePO4/C prepared using the sol-gel method, J. N. Mater. Electrochem. Syst. 17 (2014) 91–97, https://doi.org/10.14447/jnmes.v17i2.429.
[93] D.G. Tong, F.L. Luo, W. Chu, Y.L. Li, P. Wu, Effect of rhodium substitution on the electrochemical performance of LiFePO4/C, Mater. Chem. Phys. 124 (2010) 1–5, https://doi.org/10.1016/j.matchemphys.2010.05.030.
[94] Y. Gao, L. Li, H. Peng, Z. Wei, Surfactant-assisted sol-gel synthesis of nanostructured ruthenium-doped lithium iron phosphate as a cathode for lithium-ion batteries, ChemElectroChem 1 (2014) 2146–2152, https://doi.org/10.1002/celc.201402247.
[95] Z. Ma, G. Shao, G. Wang, J. Du, Y. Zhang, Electrochemical performance of Mo-doped LiFePO4/C composites prepared by two-step solid-state reaction, Ion. (Kiel.) 19 (2013) 437–443, https://doi.org/10.1007/s11581-012-0768-y.
[96] A. Jiang, X. Wang, M. Gao, J. Wang, G. Liu, W. Yu, H. Zhang, X. Dong, Enhancement of electrochemical properties of niobium-doped LiFePO4/C synthesized by sol–gel method, J. Chin. Chem. Soc. 65 (2018) 977–981, https://doi.org/10.1002/jccs.201700423.
[97] H. Liu, Q. Cao, L.J. Fu, C. Li, Y.P. Wu, H.Q. Wu, Doping effects of zinc on LiFePO4 cathode material for lithium ion batteries, Electrochem. Commun. 8 (2006) 1553–1557, https://doi.org/10.1016/j.elecom.2006.07.014.
[98] Z.R. Chang, H.J. Lv, H. Tang, X.Z. Yuan, H. Wang, Synthesis and performance of high tap density LiFePO4/C cathode materials doped with copper ions, J. Alloy. Compd. 501 (2010) 14–17, https://doi.org/10.1016/j.jallcom.2010.04.112.
[99] Q. Liu, Z. Liu, G. Xiao, S. Liao, Enhancement of capacity at high charge/discharge rate and cyclic stability of LiFePO4/C by nickel doping, Ion. (Kiel.) 19 (2013) 445–450, https://doi.org/10.1007/s11581-012-0775-z.
[100] H. Gao, L. Jiao, J. Yang, Z. Qi, Y. Wang, H. Yuan, High rate capability of Co-doped LiFePO4/C, Electrochim. Acta 97 (2013) 143–149, https://doi.org/10.1016/j.electacta.2013.02.132.
[101] J. Hu, Y. Jiang, S. Cui, Y. Duan, T. Liu, H. Guo, L. Lin, Y. Lin, J. Zheng, K. Amine, F. Pan, 3D-Printed Cathodes of LiMn1−xFexPO4 Nanocrystals Achieve Both Ultrahigh Rate and High Capacity for Advanced Lithium-Ion Battery, Adv. Energy Mater. 6 (2016), https://doi.org/10.1002/aenm.201600856.
[102] H.C. Shin, S.Bin Park, H. Jang, K.Y. Chung, W.Il Cho, C.S. Kim, B.W. Cho, Rate performance and structural change of Cr-doped LiFePO4/C during cycling, Electrochim. Acta 53 (2008) 7946–7951, https://doi.org/10.1016/j.electacta.2008.06.005.
[103] S. Jiang, Y. Wang, Synthesis and characterization of vanadium-doped LiFePO 4 @C electrode with excellent rate capability for lithium-ion batteries, Solid State Ion. 335 (2019) 97–102, https://doi.org/10.1016/j.ssi.2019.03.002.
[104] G.X. Wang, S. Bewlay, J. Yao, J.H. Ahn, S.X. Dou, H.K. Liu, Characterization of LiMxFe1-xPO4 (M=Mg, Zr, Ti) cathode materials prepared by the sol-gel method, Electrochem. Solid-State Lett. 7 (2004) A503, https://doi.org/10.1149/1.1819867.
[105] J. Ma, B. Li, H. Du, C. Xu, F. Kang, The improvement of the high-rate charge/discharge performances of LiFePO 4 cathode material by Sn doping, J. Solid State Electrochem 16 (2012) 1–8, https://doi.org/10.1007/s10008-010-1263-x.
[106] A. Kumar, P. Bashiri, B.P. Mandal, K.S. Dhindsa, K. Bazzi, A. Dixit, M. Nazri, Z. Zhou, V.K. Garg, A.C. Oliveira, P.P. Vaishnava, V.M. Naik, G.A. Nazri, R. Naik, Optimization of electrochemical performance of LiFePO4/C by indium doping and high temperature annealing, Inorganics 5 (2017) 67, https://doi.org/10.3390/inorganics5040067.
[107] A. Kulka, A. Braun, T.W. Huang, A. Wolska, M.T. Klepka, A. Szewczyk, D. Baster, W. Zając, K.-wierczek, J. Molenda, Evidence for Al doping in lithium sublattice of LiFePO4, Solid State Ion. 270 (2015) 33–38, https://doi.org/10.1016/j.ssi.2014.12.004.
[108] G.T.K. Fey, C.J. Yan, Y.C. Lin, K.P. Huang, Y.Da Cho, P.J. Wu, Y.Sen Sun, H. M. Kao, Calcium doping effects on the electrochemical properties of LiFePO 4/C cathode materials for lithium-ion batteries, Adv. Mater. Res. 560–561 (2012) 499–505, https://doi.org/10.4028/www.scientific.net/AMR.560-561.499.
[109] Z. Yang, J. Xia, L. Zhi, W. Zhang, B. Pei, An improved solid-state reaction route to Mg2+ -doped LiFePO4/C cathode material for Li-ion battery, Ion. (Kiel.) 20 (2014) 169–174, https://doi.org/10.1007/s11581-013-0974-2.
[110] X. Fang, J. Li, K. Huang, S. Liu, C. Huang, S. Zhuang, J. Zhang, Synthesis and electrochemical properties of K-doped LiFePO 4/C composite as cathode material for lithium-ion batteries, J. Solid State Electrochem 16 (2012) 767–773, https://doi.org/10.1007/s10008-011-1426-4.
[111] B. Wang, Y. Wang, H. Wu, L. Yao, L. Yang, J. Li, M. Xiang, Y. Zhang, H. Liu, Ultrafast and durable lithium storage enabled by porous bowl-like LiFePO4/C composite with Na+ doping, ChemElectroChem 4 (2017) 1141–1147, https://doi.org/10.1002/celc.201600854.
[112] J. Du, Y. Liu, X. Mo, Y. Li, J. Li, X. Wu, M. Ouyang, Impact of high-power charging on the durability and safety of lithium batteries used in long-range battery electric vehicles, Appl. Energy 255 (2019) 113793, https://doi.org/10.1016/j.apenergy.2019.113793.
[113] J. Du, W. Wang, Z. Wei, F. Hu, X. Wu, Capacity fading rules of lithium-ion batteries for multiple thermoelectric aging paths, Batteries 9 (2023) 3, https://doi.org/10.3390/batteries9010003.
[114] M. Gaberščček, Understanding Li-based battery materials via electrochemical impedance spectroscopy, Nat. Commun. 12 (2021) 6513, https://doi.org/10.1038/s41467-021-26894-5.
[115] S.D. Talian, S. Brutti, M.A. Navarra, J. Moškon, M. Gaberscek, Impedance spectroscopy applied to lithium battery materials: good practices in measurements and analyses, Energy Storage Mater. 69 (2024) 103413, https://doi.org/10.1016/j.ensm.2024.103413.
[116] N.O. Laschuk, E.B. Easton, O.V. Zenkina, Reducing the resistance for the use of electrochemical impedance spectroscopy analysis in materials chemistry, RSC Adv. 11 (2021) 27925–27936, https://doi.org/10.1039/d1ra03785d.
[117] P. Iurilli, C. Brivio, V. Wood, On the use of electrochemical impedance spectroscopy to characterize and model the aging phenomena of lithium-ion batteries: a critical review, J. Power Sources 505 (2021) 229860, https://doi.org/10.1016/j.jpowsour.2021.229860.
[118] P. Juntree, S. Siriroj, J. Padchasri, P. Songsiriritthigul, P. Kidkhunthod, Development of Li-ion batteries cathode materials by using nickel and cobalt mixed li-borate base glass composite with V2O5 via melt quenching method, J. Alloy. Compd. (2025) 178961, https://doi.org/10.1016/j.jallcom.2025.178961.
[119] L. Singh, S. Kumar, R. Kumar, V. Srivastva, M. Bechelany, Y. Lee, Insights into solid solution-assisted polyanion cathodes: present status, environmental focus and advancement in phosphate and borate chemistry for Li- and Na-ion battery technologies, J. Alloy. Compd. 1010 (2025) 177067, https://doi.org/10.1016/j.jallcom.2024.177067.